Physics of Fluids

Revisiting Reynolds and Nusselt numbers in turbulent thermal convection

Cite as: Phys. Fluids **33**, 015113 (2021); https://doi.org/10.1063/5.0032498
Submitted: 08 October 2020 . Accepted: 19 December 2020 . Published Online: 11 January 2021

Shashwat Bhattacharya, Mahendra K. Verma, and Ravi Samtaney

View Online Export Citation CrossMark

ARTICLES YOU MAY BE INTERESTED IN

Statistics of temperature and thermal energy dissipation rate in low-Prandtl number turbulent thermal convection
Physics of Fluids **31**, 125101 (2019); https://doi.org/10.1063/1.5129818

Inner and outer scales in turbulent Rayleigh–Bénard convection
Physics of Fluids **32**, 115115 (2020); https://doi.org/10.1063/5.0029853

The law of the wall: A new perspective
Physics of Fluids **32**, 121401 (2020); https://doi.org/10.1063/5.0036387

© 2021 Author(s).

Physics of Fluids ARTICLE scitation.org/journal/phf

Revisiting Reynolds and Nusselt numbers in turbulent thermal convection

Cite as: Phys. Fluids 33, 015113 (2021); doi: 10.1063/5.0032498
Submitted: 8 October 2020 • Accepted: 19 December 2020 •
Published Online: 11 January 2021

View Online Export Citation CrossMark

Shashwat Bhattacharya,[1,a)] Mahendra K. Verma,[2] and Ravi Samtaney[3]

AFFILIATIONS

[1] Department of Mechanical Engineering, Indian Institute of Technology Kanpur, Kanpur 208016, India
[2] Department of Physics, Indian Institute of Technology Kanpur, Kanpur 208016, India
[3] Mechanical Engineering, Division of Physical Science and Engineering, King Abdullah University of Science and Technology, Thuwal 23955, Saudi Arabia

[a)] **Author to whom correspondence should be addressed:** shabhatt@iitk.ac.in

ABSTRACT

In this paper, we extend Grossmann and Lohse's (GL) model [S. Grossmann and D. Lohse, "Thermal convection for large Prandtl numbers," Phys. Rev. Lett. **86**, 3316 (2001)] for the predictions of Reynolds number (Re) and Nusselt number (Nu) in turbulent Rayleigh–Bénard convection. Toward this objective, we use functional forms for the prefactors of the dissipation rates in the bulk and boundary layers. The functional forms arise due to inhibition of nonlinear interactions in the presence of walls and buoyancy compared to free turbulence, along with a deviation of the viscous boundary layer profile from Prandtl–Blasius theory. We perform 60 numerical runs on a three-dimensional unit box for a range of Rayleigh numbers (Ra) and Prandtl numbers (Pr) and determine the aforementioned functional forms using machine learning. The revised predictions are in better agreement with the past numerical and experimental results than those of the GL model, especially for extreme Prandtl numbers.

Published under license by AIP Publishing. https://doi.org/10.1063/5.0032498

I. INTRODUCTION

A classical problem in fluid dynamics is Rayleigh–Bénard convection (RBC), where a fluid is enclosed between two horizontal walls with the bottom wall kept at a higher temperature than the top wall. RBC serves as a paradigm for many types of convective flows occurring in nature and in engineering applications. RBC is primarily governed by two parameters: the Rayleigh number, Ra, which is the ratio of the buoyancy and the dissipative force, and the Prandtl number, Pr, which is the ratio of kinematic viscosity and thermal diffusivity of the fluid. In this paper, we derive a relation to predict two important quantities—the Nusselt number, Nu, and the Reynolds number, Re, which are respective measures of large-scale heat transport and velocity in turbulent RBC.

The dependence of Nu and Re on RBC's governing parameters (Ra and Pr) has been extensively studied in the literature.[1–5] Malkus[6] proposed $\mathrm{Nu} \sim \mathrm{Ra}^{1/3}$ based on marginal stability theory. For very large Ra called the ultimate regime, Kraichnan[7] deduced $\mathrm{Nu} \sim \sqrt{\mathrm{RaPr}}$, $\mathrm{Re} \sim \sqrt{\mathrm{Ra}/\mathrm{Pr}}$ for $\mathrm{Pr} \le 0.15$ and $\mathrm{Nu} \sim \sqrt{\mathrm{RaPr}^{-1/2}}$, $\mathrm{Re} \sim \sqrt{\mathrm{Ra}/\mathrm{Pr}^{3/2}}$ for $0.15 < \mathrm{Pr} \le 1$, with logarithmic corrections. Subsequently, Castaing *et al.*[8] argued that $\mathrm{Nu} \sim \mathrm{Ra}^{2/7}$ and $\mathrm{Re} \sim \mathrm{Ra}^{3/7}$ based on the existence of a mixing zone in the central region of the RBC cell, where hot rising plumes meet the mildly warm fluid. Castaing *et al.*[8] also deduced that $\mathrm{Re}^{\omega} \sim \mathrm{Ra}^{1/2}$, where Re^{ω} is the Reynolds number based on the frequency ω of torsional azimuthal oscillations of the large-scale wind in RBC. Later, Shraiman and Siggia[9] derived that $\mathrm{Nu} \sim \mathrm{Ra}^{2/7}\mathrm{Pr}^{-1/7}$ and $\mathrm{Re} \sim \mathrm{Ra}^{3/7}\mathrm{Pr}^{-5/7}$ (with logarithmic corrections) using the properties of boundary layers. They also derived exact relations between Nu and the viscous and thermal dissipation rates.

Many experiments and simulations of RBC have been performed to obtain the scaling of Nu and Re. These studies also revealed a power-law scaling of Nu and Re as $\mathrm{Nu} \sim \mathrm{Ra}^{\alpha}\mathrm{Pr}^{\beta}$ and $\mathrm{Re} \sim \mathrm{Ra}^{\gamma}\mathrm{Pr}^{\delta}$. For the scaling of Nu, the exponent α ranges from 1/4 for $\mathrm{Pr} \ll 1$ to approximately 1/3 for $\mathrm{Pr} \gtrsim 1$[8,10–29] and β from approximately zero for $\mathrm{Pr} \gtrsim 1$ to 0.14 for $\mathrm{Pr} \ll 1$.[30,31] Thus, Nu has a relatively weaker dependence on Pr. For the scaling of Re, the exponent γ was observed to be approximately 2/5 for $\mathrm{Pr} \ll 1$, 1/2 for $\mathrm{Pr} \sim 1$, and 3/5 for $\mathrm{Pr} \gg 1$;[8,10,11,15–18,22–24,32–35] and δ has been observed to range from −0.7 for $\mathrm{Pr} \lesssim 1$ to −0.95 for $\mathrm{Pr} \gg 1$.[30,36] A careful examination of the results of the above references reveals that the above exponents also depend on the regime of Ra as well. The

Published under license by AIP Publishing

ultimate regime, characterized by Nu ~ $\sqrt{\text{Ra}}$, has been observed in simulations of RBC with periodic boundary conditions,[34,37] in free convection with the density gradient,[38–40] and in convection with only lateral walls.[41] Using numerical simulations, Calzavarini *et al.*[42] showed that Re ~ $\text{Pr}^{1/2}$ and Nu ~ $\text{Pr}^{1/2}$ for convection with periodic walls. However, some doubts have been raised on the ultimate scaling observed in RBC with periodic walls because of the presence of elevator modes in the system.[43,44] Some experiments and simulations of RBC with non-periodic walls and very large Ra (~ 10^{15}) have reported a possible transition to the ultimate regime;[15,38,45,46] however, some others[47,48] argue against such transition.

The above studies show that the scaling of Re and Nu depends on the regime of Ra and Pr, highlighting the need for a unified model that encompasses all the regimes. Grossmann and Lohse[49–52] constructed one such model, henceforth referred to as the GL model. To derive this model, Grossmann and Lohse[49,50] substituted the bulk and boundary layer contributions of viscous and thermal dissipation rates in the exact relations of Shraiman and Siggia.[9] The bulk and boundary layer contributions were written in terms of Re, Nu, Ra, and Pr using the properties of boundary layers (Prandtl–Blasius theory)[53] and those of hydrodynamic and passive scalar turbulence in the bulk. Finally, using additional crossover functions, Grossmann and Lohse[50] obtained a system of equations for Re and Nu in terms of Ra, Pr, and four coefficients that were determined using inputs from experimental data.[54] Using the momentum equation of RBC, Pandey *et al.*[22,23] constructed a model to predict the Reynolds number as a function of Ra and Pr. The predictions of Kraichnan,[7] Castaing *et al.*,[8] and Shraiman and Siggia[9] are limiting cases of the GL model.

The GL model has been quite successful in predicting large-scale velocity and heat transport in many experiments and simulations. However, it does not capture large Pr convection very accurately[5] and has been reported to under-predict the Reynolds number.[1] Note that the scaling exponent for Re has a longer range (0.40–0.60) compared to that for Nu (0.25–0.33); hence, the predictions for Re are more sensitive to modeling parameters. Furthermore, the GL model is based on certain assumptions that are not valid for RBC. For example, the model assumes the viscous and the thermal dissipation rate in the bulk scale as U^3/d and $U\Delta^2/d$ (for Pr $\lesssim 1$), respectively, as in passive scalar turbulence with open boundaries.[55,56] Here, U is the large-scale velocity, and Δ and d are, respectively, the temperature difference and distance between the top and bottom walls. However, subsequent studies of RBC have shown that the aforementioned viscous and thermal dissipation rates in the bulk are suppressed by approximately $\text{Ra}^{-0.2}$ for Pr ~ 1.[11,17,22,23,57–59] The above suppression is due to the inhibition of nonlinear interactions because of walls[22,23] and buoyancy.[60] Moreover, recent studies have revealed that the viscous boundary layer thickness in RBC considerably deviate from $\text{Re}^{-1/2}$ as assumed in the GL model.[58,61,62]

In the present work, we address the above limitations of the GL model and propose a new relation for the Reynolds and Nusselt numbers involving a cubic polynomial equation for Re and Nu. For implementation of the viscous and thermal dissipation rates in the bulk and boundary layers, we employ machine-learning tools on 60 datasets that were obtained using numerical simulations of RBC. The new relation rectifies some of the limitations of the GL model, especially for small and large Prandtl numbers.

The outline of the paper is as follows: In Sec. II, we discuss the governing equations of RBC and briefly explain the GL model. Then, we extend the GL framework by using functional forms for the prefactors of the dissipation rates in the bulk and boundary layers and incorporate the deviation in the scaling of viscous boundary layer thickness described earlier. Simulation details are provided in Sec. III. In Sec. IV, we report the scaling of boundary layer thicknesses and dissipation rates using our data, following which we describe the machine-learning tools used to determine the aforementioned functional forms. We also test the revised predictions with experiments and numerical simulations, and compare them with those of the GL model. We conclude in Sec. V.

II. RBC EQUATIONS AND THE GL MODEL

We consider RBC under the Boussinesq approximation, whose governing equations are as follows:[5,63]

$$\frac{\partial \mathbf{u}}{\partial t} + (\mathbf{u}\cdot\nabla)\mathbf{u} = -\nabla p/\rho_0 + \alpha g T\hat{z} + \nu\nabla^2\mathbf{u}, \tag{1}$$

$$\frac{\partial T}{\partial t} + (\mathbf{u}\cdot\nabla)T = \kappa\nabla^2 T, \tag{2}$$

$$\nabla\cdot\mathbf{u} = 0, \tag{3}$$

where $\mathbf{u}$ and p are the velocity and pressure fields, respectively, T is the temperature field, ν is the kinematic viscosity, κ is the thermal diffusivity, α is the thermal expansion coefficient, ρ_0 is the mean density of the fluid, and g is the acceleration due to gravity.

Using d as the length scale, $\sqrt{\alpha g\Delta d}$ as the velocity scale, and Δ as the temperature scale, we non-dimensionalize Eqs. (1)–(3) that yield

$$\frac{\partial \mathbf{u}}{\partial t} + \mathbf{u}\cdot\nabla\mathbf{u} = -\nabla p + T\hat{z} + \sqrt{\frac{\text{Pr}}{\text{Ra}}}\nabla^2\mathbf{u}, \tag{4}$$

$$\frac{\partial T}{\partial t} + \mathbf{u}\cdot\nabla T = \frac{1}{\sqrt{\text{RaPr}}}\nabla^2 T, \tag{5}$$

$$\nabla\cdot\mathbf{u} = 0, \tag{6}$$

where $\text{Ra} = \alpha g\Delta d^3/(\nu\kappa)$ is the Rayleigh number and $\text{Pr} = \nu/\kappa$ is the Prandtl number. The large-scale velocity and heat transfer are quantified by two important non-dimensional quantities, namely, the Reynolds number (Re) and the Nusselt number (Nu). The Nusselt number, Nu, is the ratio of the total heat flux to the conductive heat flux and is defined as $\text{Nu} = 1 + \langle u_z T\rangle/(\kappa\Delta/d)$. The Reynolds number Re is defined as $\text{Re} = Ud/\nu$, where U is the large-scale velocity. In our work, we will consider U to be the root mean square (rms) velocity, that is, $U = \sqrt{\langle u_x^2 + u_y^2 + u_z^2\rangle}$, where $\langle\cdot\rangle$ represents the volume average.

The dissipation rates of kinetic and thermal energies, represented as ϵ_u and ϵ_T, respectively, are important quantities in our study. These are defined as $\epsilon_u = 2\nu\langle S_{ij}S_{ij}\rangle$ and $\epsilon_T = \kappa\langle|\nabla T|^2\rangle$, where S_{ij} is the strain rate tensor. Shraiman and Siggia[9] derived two exact relations between Nu and the dissipation rates; these are

$$\epsilon_u = \frac{\nu^3}{d^4}(\text{Nu}-1)\frac{\text{Ra}}{\text{Pr}^2}, \tag{7}$$

Published under license by AIP Publishing

$$\epsilon_T = \frac{\kappa\Delta^2}{d^2}\mathrm{Nu}. \tag{8}$$

The above relations will be the backbone of our present work.

Now, we will briefly summarize the GL model to predict Nu and Re. Grossmann and Lohse[49,50] split the total viscous and thermal dissipation rates ($\tilde{D}_u = \epsilon_u V$ and $\tilde{D}_T = \epsilon_T V$, respectively, V being the domain volume) into their bulk and boundary layer contributions. Thus,

$$\tilde{D}_u = \tilde{D}_{u,\mathrm{bulk}} + \tilde{D}_{u,\mathrm{BL}}, \tag{9}$$

$$\tilde{D}_T = \tilde{D}_{T,\mathrm{bulk}} + \tilde{D}_{T,\mathrm{BL}}. \tag{10}$$

The GL model assumes the Prandtl–Blasius relation of $\delta_u \sim \mathrm{Re}^{-1/2}$ above a critical Reynolds number Re_c for viscous boundary layers and $\delta_T = d/2\mathrm{Nu}$ for thermal boundary layers. Here, δ_u and δ_T are the viscous and thermal boundary layer thicknesses, respectively. For $\mathrm{Re} < \mathrm{Re}_c$, the viscous boundary layer is assumed to occupy the entire RBC cell. Using the above relations and the properties of hydrodynamic and passive scalar turbulence in the bulk (see Sec. IV A), Grossmann and Lohse[49,50] deduced that

$$\frac{1}{V}\tilde{D}_{u,\mathrm{bulk}} \sim \frac{U^3}{d} = c_1\frac{\nu^3}{d^4}\mathrm{Re}^3, \tag{11}$$

$$\frac{1}{V}\tilde{D}_{u,\mathrm{BL}} \sim \frac{\nu U^2}{\delta_u^2}\frac{\delta_u}{d} = c_2\frac{\nu^3}{d^4}\mathrm{Re}^{2.5}, \tag{12}$$

$$\frac{1}{V}\tilde{D}_{T,\mathrm{bulk}} \sim \frac{U\Delta^2}{d} = c_3\frac{\kappa\Delta^2}{d^2}\mathrm{RePr}, \tag{13}$$

$$\frac{1}{V}\tilde{D}_{T,\mathrm{BL}} \sim \frac{\kappa\Delta^2}{\delta_T^2}\frac{\delta_T}{d} = c_4\frac{\kappa\Delta^2}{d^2}\mathrm{Nu}, \tag{14}$$

where c_1, c_2, c_3, and c_4 are constants. Note that for $\delta_u > \delta_T$ ($\mathrm{Pr} \gg 1$), Grossmann and Lohse[49] modified Eq. (13) as

$$\frac{1}{V}\tilde{D}_{T,\mathrm{bulk}} \sim \frac{\delta_T}{\delta_u}\frac{U\Delta^2}{d} = c_3\frac{\kappa\Delta^2}{d}\mathrm{Re}^{3/2}\mathrm{PrNu}^{-1}. \tag{15}$$

By approximating the dominant terms of Eq. (2) in the thermal boundary layers, Grossmann and Lohse[49,50] further deduced that $\mathrm{Nu} \sim \mathrm{Re}^{1/2}\mathrm{Pr}^{1/2}$ for $\delta_u < \delta_T$ and $\mathrm{Nu} \sim \mathrm{Re}^{1/2}\mathrm{Pr}^{1/3}$ for $\delta_u > \delta_T$. To ensure smooth transition through different regimes of boundary layer thicknesses and Reynolds number, Grossmann and Lohse[50] introduced two crossover functions, $f(x) = (1+x^4)^{-1/4}$ and $g(x) = x(1+x^4)^{-1/4}$, and applied them in the RHS of Eqs. (12)–(15). Finally, Grossmann and Lohse[50] put the modeling and splitting assumptions [Eqs. (9)–(15)] together with the exact relations given by Eqs. (7) and (8) to obtain the following set of equations for Nu and Re:

$$(\mathrm{Nu}-1)\frac{\mathrm{Ra}}{\mathrm{Pr}^2} = c_1\mathrm{Re}^3 + c_2\frac{\mathrm{Re}^2}{g(\sqrt{\mathrm{Re}_c/\mathrm{Re}})}, \tag{16}$$

$$\mathrm{Nu} = c_3\mathrm{PrRe}f\left[\frac{2a\mathrm{Nu}}{\sqrt{\mathrm{Re}_c}}g\left(\sqrt{\frac{\mathrm{Re}_c}{\mathrm{Re}}}\right)\right] + c_4\sqrt{\mathrm{RePr}}\left\{f\left[\frac{2a\mathrm{Nu}}{\sqrt{\mathrm{Re}_c}}g\left(\sqrt{\frac{\mathrm{Re}_c}{\mathrm{Re}}}\right)\right]\right\}^{1/2}. \tag{17}$$

The values of the constants, obtained from experiments, are $c_1 = 1.38$, $c_2 = 8.05$, $c_3 = 0.0252$, $c_4 = 0.487$, $a = 0.922$, and $\mathrm{Re}_c = 3.401$.[54] The above equations can be solved iteratively to obtain Re and Nu for given Ra and Pr.

Although the GL model has been quite successful in predicting Re and Nu, it has certain deficiencies due to some assumptions that are invalid for RBC. First, recent studies reveal that the relation $\delta_u \sim \mathrm{Re}^{-1/2}$ for the viscous boundary layers is not strictly valid for RBC.[58,61,62] The viscous boundary layer thickness becomes a progressively weaker function of Re as Pr is increased.[64] Thus, the relation given by Eq. (12) is not accurate. Second, as discussed earlier, studies have shown that for $\mathrm{Pr} \sim 1$, the thermal and viscous dissipation rates in the bulk are suppressed relative to free turbulence,[17,57–59]

$$\frac{1}{V}\tilde{D}_{u,\mathrm{bulk}} \sim \frac{U^3}{d}\mathrm{Ra}^{-0.18}, \quad \frac{1}{V}\tilde{D}_{T,\mathrm{bulk}} \sim \frac{U\Delta^2}{d}\mathrm{Ra}^{-0.20}.$$

Contrast the above relations with Eqs. (11) and (13)[58,59] used in the GL model. This clearly signifies that c_1 and c_3 from Eqs. (11) and (13) cannot be treated as constants. Thus, it becomes imperative to study how c_i varies with Ra and Pr in different regimes of RBC.

We propose a modified relation for Re and Nu by incorporating the aforementioned suppression of the total dissipation rates, as well as the modified law for the viscous boundary layers. Toward this objective, we make the following modifications to Eqs. (11)–(14),

$$\frac{1}{V}\tilde{D}_{u,\mathrm{bulk}} = f_1(\mathrm{Ra},\mathrm{Pr})\frac{U^3}{d} = f_1(\mathrm{Ra},\mathrm{Pr})\frac{\nu^3}{d^4}\mathrm{Re}^3, \tag{18}$$

$$\frac{1}{V}\tilde{D}_{u,\mathrm{BL}} = f_2(\mathrm{Ra},\mathrm{Pr})\frac{\nu U^2}{\delta_u^2}\frac{\delta_u}{d} = f_2(\mathrm{Ra},\mathrm{Pr})\frac{\nu^3}{d^4}\frac{d}{\delta_u}\mathrm{Re}^2, \tag{19}$$

$$\frac{1}{V}\tilde{D}_{T,\mathrm{bulk}} = f_3(\mathrm{Ra},\mathrm{Pr})\frac{U\Delta^2}{d} = f_3(\mathrm{Ra},\mathrm{Pr})\frac{\kappa\Delta^2}{d^2}\mathrm{RePr}, \tag{20}$$

$$\frac{1}{V}\tilde{D}_{T,\mathrm{BL}} = f_4(\mathrm{Ra},\mathrm{Pr})\frac{\kappa\Delta^2}{\delta_T^2}\frac{\delta_T}{d} = f_4(\mathrm{Ra},\mathrm{Pr})\frac{\kappa\Delta^2}{d^2}\mathrm{Nu}. \tag{21}$$

Note that we replaced the coefficients c_i with functions $f_i(\mathrm{Ra},\mathrm{Pr})$. Furthermore, we do not express d/δ_u in terms of Re in Eq. (19). The above modified formulas are inserted in the exact relations of Shraiman and Siggia[9] that lead to

$$(\mathrm{Nu}-1)\frac{\mathrm{Ra}}{\mathrm{Pr}^2} = f_1(\mathrm{Ra},\mathrm{Pr})\mathrm{Re}^3 + f_2(\mathrm{Ra},\mathrm{Pr})\frac{d}{\delta_u}\mathrm{Re}^2, \tag{22}$$

$$\mathrm{Nu} = f_3(\mathrm{Ra},\mathrm{Pr})\mathrm{RePr} + 2f_4(\mathrm{Ra},\mathrm{Pr})\mathrm{Nu}. \tag{23}$$

The functions $f_i(\mathrm{Ra},\mathrm{Pr})$ will be later determined using our simulation results. For the sake of brevity, we will skip the arguments within the parenthesis of f_i's henceforth.

Equations (22) and (23) constitute a system of two equations with two unknowns (Re and Nu). To solve these equations, we will now reduce them to a cubic polynomial equation for Re by eliminating Nu. We rearrange Eq. (23) to obtain

$$\mathrm{Nu} = \frac{f_3}{1-2f_4}\mathrm{RePr}. \tag{24}$$

Published under license by AIP Publishing

Substitution of Eq. (24) in Eq. (22) yields the following cubic equation for Re:

$$f_1\mathrm{Re}^3 + f_2\frac{d}{\delta_u}\mathrm{Re}^2 - \frac{f_3}{1-2f_4}\frac{\mathrm{Ra}}{Pr}\mathrm{Re} + \frac{\mathrm{Ra}}{\mathrm{Pr}^2} = 0. \tag{25}$$

The above equation for Re can be solved for a given Ra and Pr once f_i and δ_u have been determined. We determine Nu using Eq. (24) once Re has been computed.

Now, we will show that in the limit of the viscous dissipation rate dominating in the bulk or in the boundary layers ($\tilde{D}_{u,\mathrm{bulk}} \gg \tilde{D}_{u,\mathrm{BL}}$ or vice versa), Eqs. (22) and (23) are reduced to power-law expressions for Re and Nu. In the following discussion, we consider scaling for these limiting cases.

Case 1: $\tilde{D}_{u,\mathrm{bulk}} \gg \tilde{D}_{u,\mathrm{BL}}$

First, let us consider the case where the viscous dissipation rate in the bulk is dominant. This regime is expected for large Ra ($\gg 10^8$) or for small Pr ($\ll 1$), where the boundary layers are thin. In this regime, $f_2(d/\delta_u)\mathrm{Re}^2 \ll f_1\mathrm{Re}^3$. Assuming Nu $\gg 1$, Eq. (22) reduces to

$$\mathrm{Nu}\frac{\mathrm{Ra}}{\mathrm{Pr}^2} \approx f_1\mathrm{Re}^3. \tag{26}$$

Using Eqs. (24) and (26), we arrive at

$$\mathrm{Re} = \sqrt{\frac{f_3}{f_1(1-2f_4)}\frac{\mathrm{Ra}}{\mathrm{Pr}}}, \tag{27}$$

$$\mathrm{Nu} = \sqrt{\frac{1}{f_1}\left(\frac{f_3}{1-2f_4}\right)^3\mathrm{RaPr}}. \tag{28}$$

Note that f_1 and f_3 are expected to be constants and $f_4 \approx 0$ when the boundary layers are absent (as in a periodic box) or weak (as in the ultimate regime proposed by Kraichnan[7]). For this case, $\mathrm{Re} \sim \sqrt{\mathrm{Ra}/\mathrm{Pr}}$ and $\mathrm{Nu} \sim \sqrt{\mathrm{RaPr}}$, consistent with the arguments of Kraichnan[7] for large Ra and small Pr. However, for RBC with walls, the relations for Re and Nu will deviate from the above relations because f_1 and f_3 are functions of Ra and Pr.

Case 2: $\tilde{D}_{u,\mathrm{BL}} \gg \tilde{D}_{u,\mathrm{bulk}}$

Now, we consider the other extreme when the viscous dissipation rates in the boundary layers are dominant, which is expected for small Ra ($\ll 10^5$) or for large Pr ($\gg 7$).[49,50,57] In this regime, again assuming Nu $\gg 1$, Eq. (22) reduces to

$$\mathrm{Nu}\frac{\mathrm{Ra}}{\mathrm{Pr}^2} \approx f_2\frac{d}{\delta_u}\mathrm{Re}^2. \tag{29}$$

Using Eqs. (24) and (29), we obtain

$$\mathrm{Re} = \left\{\frac{f_3}{f_2(1-2f_4)}\frac{\delta_u}{d}\right\}\frac{\mathrm{Ra}}{\mathrm{Pr}}, \tag{30}$$

$$\mathrm{Nu} = \frac{1}{f_2}\frac{\delta_u}{d}\left(\frac{f_3}{1-2f_4}\right)^2\mathrm{Ra}. \tag{31}$$

We will examine these cases once we deduce the forms of f_i using our numerical simulations.

We remark that the aspect ratio of the RBC cell also influences the scaling of Ra and Pr.[52] In the current work, we do not consider the effect of aspect ratio. We intend to include the aspect ratio dependence in a future work.

In Sec. III, we will discuss the simulation method.

III. SIMULATION DETAILS

We perform direct numerical simulations of RBC by solving Eqs. (4)–(6) in a cubical box of unit dimensions using the finite difference code SARAS.[66,67] We carry out 60 runs for Pr ranging from 0.02 to 100 and Ra ranging from 5×10^5 to 5×10^9. The grid size was varied from 257^3 to 1025^3 depending on parameters. Refer to Tables I and II for the simulation details.

We impose isothermal boundary conditions on the horizontal walls and adiabatic boundary conditions on the sidewalls. No-slip boundary conditions were imposed on all the walls. A second-order Crank–Nicholson scheme was used for time-advancement, with the maximum Courant number kept at 0.2. The solver uses a multigrid method for solving the pressure-Poisson equations. We ensure a minimum of five points in the viscous and thermal boundary layers (see Tables I and II); this satisfies the resolution criterion of Grötzbach,[68] and Verzicco and Camussi.[57] The simulations are run up to 3–263 non-dimensional time units (t_{ND}) after attaining a steady state. For post-processing, we employ a central difference method for spatial differentiation and Simpson's method for computing the volume average.

In order to resolve the smallest scales of the flow, we ensure that the grid spacing Δx is smaller than the Kolmogorov length scale $\eta = (\nu^3\epsilon_u^{-1})^{1/4}$ for $\mathrm{Pr} \le 1$ and the Batchelor length scale $\eta_T = (\nu\kappa^2\epsilon_u^{-1})^{1/4}$ for $\mathrm{Pr} > 1$. We numerically compute ϵ_u and ϵ_T and use these values to compute Nu_u and Nu_T employing Shraiman and Siggia's exact relations[9] [see Eqs. (7) and (8)]. The Nusselt numbers computed using $\langle u_z T\rangle$ match with Nu_u and Nu_T within two percent on an average; this further confirms that our runs are well-resolved (see Tables I and II). All the above quantities are averaged over 12 to 259 snapshots taken at equal time intervals after attaining a steady state.

In Sec. IV, we analyze our numerical results, construct the cubic polynomial relation for Re and Nu using the data from our simulations, and compare our revised predictions with those of the GL model.

IV. RESULTS

Using our numerical data, we determine the scaling of dissipation rates, boundary layer thicknesses, and the functional forms of f_i. We construct the relations for Re and Nu given by Eqs. (22) and (23) using these inputs and compare the revised predictions with those of the original GL model. We also analyze how the proposed relation performs in the limit of $\tilde{D}_{u,\mathrm{bulk}} \gg \tilde{D}_{u,\mathrm{BL}}$ and vice versa.

A. Viscous and thermal dissipation rates

Here, we examine the scaling of viscous and thermal dissipation rates and explore how their scaling deviates from that of free turbulence. First, we present theoretical arguments on the above scaling, following which we verify our arguments with our numerical results.

Published under license by AIP Publishing

TABLE I. Details of our direct numerical simulations performed in a cubical box for Pr ≤ 1: the Prandtl number (Pr), the Rayleigh Number (Ra), the grid size, the ratio of the Kolmogorov length scale[65] (η) to the mesh width Δx, the number of grid points in viscous and thermal boundary layers (N_{VBL} and N_{TBL}, respectively), the Reynolds number (Re), the Nusselt number computed using $\langle u_z T\rangle$ and the exact relations given by Eqs. (7) and (8) (Nu, Nu_u, and Nu_T, respectively), the ratio of the total viscous dissipation rate in the boundary layer ($\tilde{D}_{u,\mathrm{BL}}$) and that in the bulk ($\tilde{D}_{u,\mathrm{bulk}}$), the ratio of the total thermal dissipation rate in the boundary layer ($\tilde{D}_{T,\mathrm{BL}}$) and that in the bulk ($\tilde{D}_{T,\mathrm{bulk}}$), and the number of non-dimensional time units (t_{ND}) and snapshots over which the quantities are averaged.

Pr	Ra	Grid size	$\eta/\Delta x$	N_{VBL}	N_{TBL}	Re	Nu	Nu_u	Nu_T	$\frac{\tilde{D}_{u,\mathrm{BL}}}{\tilde{D}_{u,\mathrm{bulk}}}$	$\frac{\tilde{D}_{T,\mathrm{BL}}}{\tilde{D}_{T,\mathrm{bulk}}}$	t_{ND}	Snapshots
0.02	5×10^5	513^3	1.99	7	58	2440	4.48	4.54	4.49	0.751	2.90	95	95
0.02	1×10^6	513^3	1.55	6	46	3200	5.78	5.79	5.78	0.564	2.89	41	41
0.02	2×10^6	513^3	1.24	5	38	4290	6.90	6.88	6.91	0.468	2.72	30	30
0.02	5×10^6	1025^3	1.81	7	59	6650	8.85	9.18	8.89	0.381	2.68	7	71
0.02	1×10^7	1025^3	1.45	7	48	9420	10.3	11.0	10.8	0.357	2.62	3	31
0.1	5×10^5	513^3	4.06	11	43	749	6.11	6.11	6.11	0.911	2.89	107	107
0.1	1×10^6	513^3	3.23	9	36	1030	7.34	7.39	7.35	0.787	2.71	66	66
0.1	2×10^6	513^3	2.58	7	30	1380	8.85	8.83	8.86	0.646	2.66	88	88
0.1	5×10^6	513^3	1.91	6	24	2090	11.3	11.4	11.3	0.539	2.63	83	83
0.1	1×10^7	513^3	1.52	6	20	2870	13.9	14.0	13.9	0.474	2.63	33	66
0.1	2×10^7	513^3	1.22	5	17	3870	16.4	16.4	16.4	0.389	2.41	37	73
0.1	5×10^7	1025^3	1.83	7	25	6020	20.8	20.8	21.3	0.337	2.22	12	12
0.1	1×10^8	1025^3	1.45	6	21	8140	26.7	26.1	26.3	0.288	2.28	5	26
0.5	1×10^6	513^3	6.96	13	32	285	8.38	8.36	8.37	1.01	3.25	71	71
0.5	3×10^6	513^3	4.85	10	24	482	11.4	11.4	11.4	0.745	2.94	140	140
0.5	1×10^7	513^3	3.28	8	17	874	15.9	16.0	16.0	0.682	2.95	91	91
0.5	3×10^7	513^3	2.30	7	13	1480	21.6	21.8	21.6	0.550	2.73	48	48
0.5	1×10^8	513^3	1.55	5	9	2610	30.6	30.8	30.6	0.475	2.58	37	37
1	1×10^6	257^3	4.92	7	17	147	8.18	8.45	8.48	0.765	2.83	101	101
1	2×10^6	257^3	3.94	7	14	213	10.1	10.1	10.2	0.791	2.98	101	101
1	5×10^6	257^3	2.90	6	11	340	13.3	13.3	13.4	0.709	2.97	101	101
1	1×10^7	257^3	2.31	5	9	491	16.3	16.3	16.4	0.679	2.93	101	101
1	2×10^7	257^3	1.85	5	7	702	19.8	19.7	19.9	0.682	2.91	91	91
1	5×10^7	513^3	2.73	7	11	1100	26.0	26.0	26.1	0.561	2.81	103	103
1	1×10^8	513^3	2.19	6	9	1530	31.4	31.3	31.5	0.512	2.69	101	101
1	2×10^8	513^3	1.75	6	8	2170	38.6	38.3	38.7	0.490	2.68	101	101
1	5×10^8	513^3	1.30	5	6	3330	49.2	49.6	49.2	0.437	2.51	101	101
1	1×10^9	1025^3	2.06	7	9	4700	61.2	61.6	61.4	0.426	2.35	15	30
1	2×10^9	1025^3	1.62	7	8	6580	76.8	81.1	76.7	0.392	2.47	13	26

In free turbulence, the viscous and scalar dissipation rates are estimated as follows:

$$\epsilon_u \sim \frac{U^3}{d}, \quad \epsilon_T \sim \frac{U\Delta^2}{d}. \tag{32}$$

However, in wall-bounded convection, the scaling of the dissipation rates is different. To understand this, let us rewrite the exact relations of Shraiman and Siggia[9] given by Eqs. (7) and (8) as

$$\epsilon_u = \frac{U^3}{d}\frac{1}{\mathrm{Re}^3}(\mathrm{Nu}-1)\frac{\mathrm{Ra}}{\mathrm{Pr}^2}, \tag{33}$$

$$\epsilon_T = \frac{U\Delta^2}{d}\frac{1}{\mathrm{RePr}}\mathrm{Nu}. \tag{34}$$

Recall from Sec. I that the Reynolds number scales as $\mathrm{Re} \sim \mathrm{Ra}^{1/2}$ for $\mathrm{Pr} \sim 1$ and $\mathrm{Re} \sim \mathrm{Ra}^{0.6}$ for $\mathrm{Pr} \gg 1$, and the Nusselt number scales as $\mathrm{Nu} \sim \mathrm{Ra}^{0.3}$ for $\mathrm{Pr} \gtrsim 1$. Substituting the above relations in Eqs. (33) and (34) yields

$$\epsilon_u \sim \begin{cases} \frac{U^3}{d}\mathrm{Ra}^{-0.2}, & \mathrm{Pr} \sim 1, \\ \frac{U^3}{d}\mathrm{Ra}^{-0.5}, & \mathrm{Pr} \gg 1, \end{cases} \tag{35}$$

instead of U^3/d, and

$$\epsilon_T \sim \begin{cases} \frac{U\Delta^2}{d}\mathrm{Ra}^{-0.2}, & \mathrm{Pr} \sim 1, \\ \frac{U\Delta^2}{d}\mathrm{Ra}^{-0.3} & \mathrm{Pr} \gg 1, \end{cases} \tag{36}$$

instead of $U\Delta^2/d$. Pandey and Verma[22] and Pandey *et al.*[23] argued that the additional Ra dependence is due to the suppression of nonlinear interactions due to the presence of walls. Some Fourier

Published under license by AIP Publishing

TABLE II. Details of our direct numerical simulations performed in a cubical box for Pr > 1: the Prandtl number (Pr), the Rayleigh Number (Ra), the grid size, the ratio of the Batchelor length scale[65] (η_T) to the mesh width Δx, the number of grid points in viscous and thermal boundary layers (N_{VBL} and N_{TBL}, respectively), the Reynolds number (Re), the Nusselt number computed using $\langle u_z T\rangle$ and the exact relations given by Eqs. (7) and (8) (Nu, Nu_u, and Nu_T, respectively), the ratio of the total viscous dissipation rate in the boundary layer ($\tilde{D}_{u,\mathrm{BL}}$) and that in the bulk ($\tilde{D}_{u,\mathrm{bulk}}$), the ratio of the total thermal dissipation rate in the boundary layer ($\tilde{D}_{T,\mathrm{BL}}$) and that in the bulk ($\tilde{D}_{T,\mathrm{bulk}}$), and the number of non-dimensional time units (t_{ND}) and snapshots over which the quantities are averaged.

Pr	Ra	Grid size	$\eta_T/\Delta x$	N_{VBL}	N_{TBL}	Re	Nu	Nu_u	Nu_T	$\frac{\tilde{D}_{u,\mathrm{BL}}}{\tilde{D}_{u,\mathrm{bulk}}}$	$\frac{\tilde{D}_{T,\mathrm{BL}}}{\tilde{D}_{T,\mathrm{bulk}}}$	t_{ND}	Snapshots
6.8	1×10^6	257^3	5.02	9	17	24.9	7.90	7.87	7.87	0.822	3.08	101	101
6.8	2×10^6	257^3	4.01	8	15	35.6	9.46	9.43	9.48	0.744	2.94	101	101
6.8	5×10^6	257^3	2.93	7	11	59.7	12.9	12.9	13.0	0.646	2.97	101	101
6.8	1×10^7	257^3	2.33	6	9	89.2	15.9	15.8	16.0	0.605	2.93	101	101
6.8	2×10^7	257^3	1.85	6	8	128	19.5	19.4	19.3	0.579	2.97	107	101
6.8	5×10^7	257^3	1.37	5	6	217	26.1	25.7	25.9	0.588	2.99	101	101
6.8	1×10^8	513^3	2.18	8	9	314	31.6	31.6	31.7	0.614	2.85	56	56
6.8	2×10^8	513^3	1.75	7	8	452	38.5	37.7	39.3	0.529	2.84	26	51
6.8	5×10^8	513^3	1.29	7	6	729	50.5	50.4	50.8	0.521	2.83	58	58
6.8	1×10^9	1025^3	2.06	11	9	1070	65.7	61.9	62.0	0.518	2.69	14	28
6.8	2×10^9	1025^3	1.64	10	8	1520	77.0	77.6	77.5	0.463	2.83	20	40
6.8	5×10^9	1025^3	1.22	9	6	2400	101	101	101	0.440	2.72	17	33
50	1×10^6	513^3	9.92	17	33	3.53	8.17	8.16	7.99	0.815	3.23	131	131
50	2×10^6	513^3	7.96	16	27	5.19	9.66	9.60	9.61	0.722	3.42	51	51
50	5×10^6	513^3	5.74	14	20	9.38	13.8	13.7	13.5	0.627	3.19	130	130
50	1×10^7	513^3	4.58	13	17	14.0	16.7	16.7	16.2	0.581	3.12	65	65
50	2×10^7	513^3	3.67	12	14	21.1	20.2	20.1	20.0	0.525	3.13	55	55
50	5×10^7	513^3	2.72	11	11	35.2	26.4	26.2	26.0	0.489	3.07	57	57
50	1×10^8	513^3	2.18	10	9	50.8	31.8	31.6	31.6	0.436	2.92	111	111
50	2×10^8	513^3	1.74	9	8	76.4	38.7	38.8	38.7	0.433	3.10	101	101
50	5×10^8	513^3	1.29	9	6	137	51.8	51.6	50.4	0.481	2.88	62	62
50	1×10^9	513^3	1.03	8	5	202	61.5	63.0	69.3	0.599	2.79	101	101
100	1×10^6	257^3	5.01	10	17	1.80	7.94	7.93	7.94	1.04	3.41	259	259
100	2×10^6	257^3	3.91	9	14	2.78	10.4	10.3	10.2	0.862	3.42	263	263
100	5×10^6	257^3	2.87	8	10	4.90	13.9	13.9	14.0	0.731	3.36	153	153
100	1×10^7	257^3	2.30	7	9	7.02	16.8	16.7	16.6	0.585	3.30	101	101
100	2×10^7	257^3	1.84	7	7	9.91	20.1	20.0	19.9	0.485	3.00	101	101
100	5×10^7	257^3	1.37	6	6	17.1	26.1	25.9	26.1	0.467	3.20	101	101
100	1×10^8	513^3	2.18	10	9	26.0	31.8	31.7	31.7	0.433	2.96	107	107
100	2×10^8	513^3	1.74	9	8	37.5	39.1	38.8	38.8	0.373	3.08	108	108
100	5×10^8	513^3	1.30	10	6	71.4	49.7	49.2	50.3	0.429	2.95	86	86

modes that are otherwise present in free turbulence are absent in wall-bounded RBC; this results in several channels of nonlinear interactions and energy cascades to be blocked.[5] Note that the horizontal walls seem to have a more pronounced effect on the aforementioned suppression than the lateral walls, as Schmidt *et al.*[41] observed passive scalar scaling for homogeneous laterally confined RBC. In addition, buoyancy also appears to suppress the energy cascade rate,[60] similar to the role played by the magnetic field in magnetohydrodynamic turbulence.[69]

Now, for Pr $\ll 1$, recall that Re $\sim \mathrm{Ra}^{0.42}$ and Nu $\sim \mathrm{Ra}^{0.25}$ (see Sec. I). Substitution of these expressions in Eqs. (33) and (34) yields

$$\epsilon_u \sim \frac{U^3}{d}, \quad \epsilon_T \sim \frac{U\Delta^2}{d}\mathrm{Ra}^{-0.17}. \tag{37}$$

Thus, the viscous dissipation rate scales similar to free turbulence for small Pr. However, the additional Ra dependence is still present in the scaling of thermal dissipation rates because of the presence of thick thermal boundary layers.

Using our data, we numerically compute the viscous and thermal dissipation rates and normalize them with U^3/d and $U\Delta^2/d$, respectively. We plot the normalized dissipation rates vs Ra and exhibit these plots in Figs. 1(a) and 1(b). We observe that for small Pr, the normalized viscous dissipation rate is independent of Ra, whereas for larger Pr, the aforementioned quantity decreases with Ra. The decrease becomes steeper as Pr increases, with $\epsilon_u/(U^3d^{-1}) \sim \mathrm{Ra}^{-0.21}$ for Pr = 1 and $\sim \mathrm{Ra}^{-0.45}$ for Pr = 100. The normalized thermal dissipation rate decreases with Ra for all Pr values, with $\epsilon_T/(U\Delta^2d^{-1}) \sim \mathrm{Ra}^{-0.15}$ for Pr = 0.02 to $\sim \mathrm{Ra}^{-0.28}$ for Pr = 100, which are consistent with the earlier estimates.

Published under license by AIP Publishing

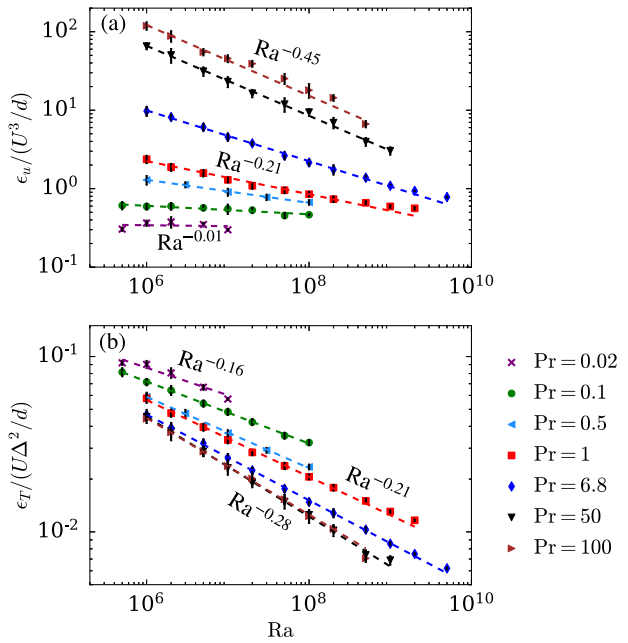

FIG. 1. Plots of (a) normalized viscous dissipation rate vs Ra and (b) normalized thermal dissipation rate vs Ra. The error bars represent the standard deviation of the dataset with respect to the temporal average. Both the viscous and thermal dissipation rates exhibit additional Ra dependence.

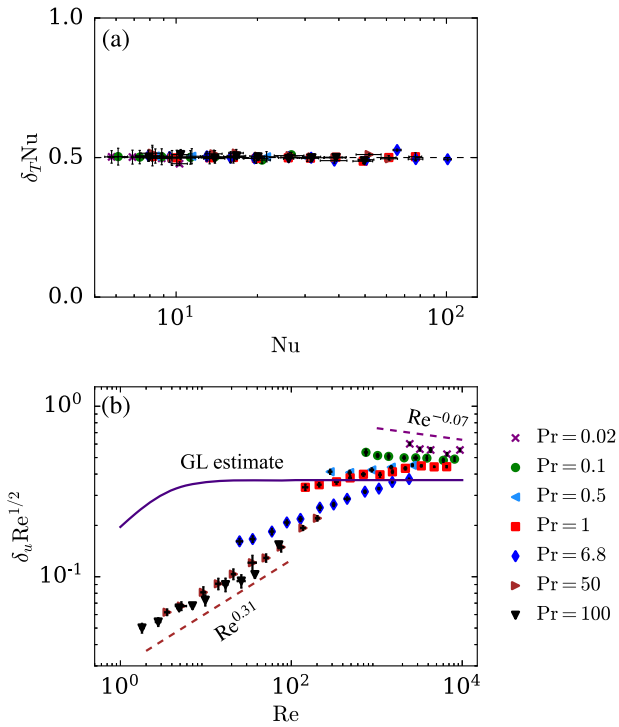

FIG. 2. Plots of (a) normalized thermal boundary layer thickness vs Nu and (b) normalized viscous boundary layer thickness vs Re. The error bars represent the standard deviation of the dataset with respect to the temporal average. The viscous boundary layer thickness deviates from the Prandtl–Blasius relation of $\delta_u \sim \mathrm{Re}^{-1/2}$, as well as from Grossmann and Lohse's estimate of $g(\sqrt{\mathrm{Re}_c/\mathrm{Re}})$.

In Subsection IV B, we discuss the computations of the boundary layer thicknesses and their dependence on Re and Nu for different Pr.

B. Boundary layer thicknesses

There are several ways to define the viscous and thermal boundary layer thicknesses in RBC.[1,61] In our paper, the viscous boundary layer thickness δ_u is defined as the depth where a linear fit of the velocity profile near the wall intersects with the tangent to the velocity profile at its local maximum. Similarly, the thermal boundary layer thickness δ_T is defined as the depth where a linear fit of the temperature profile near the wall intersects with the mean temperature $T = 0.5$. The above methods are described in detail in Refs. 1, 61, and 64.

Using the data generated from our simulations, we first compute the thicknesses of the thermal and viscous boundary layers. We report the average thicknesses of the viscous boundary layers near all the six walls and the thermal boundary layers near the top and bottom walls. We examine the validity of the Prandtl–Blasius relation of $\delta_u \sim \mathrm{Re}^{-0.5}$ for the viscous boundary layers and $\delta_T = 0.5\mathrm{Nu}^{-1}$ for the thermal boundary layers. Toward this objective, we plot $\delta_T\mathrm{Nu}$ vs Nu in Fig. 2(a) and $\delta_u\mathrm{Re}^{1/2}$ vs Re in Fig. 2(b).

We observe from Fig. 2(a) that $\delta_T\mathrm{Nu} \approx 1/2$, independent of Nu, which is consistent with the definition. On the other hand, from Fig. 2(b), it is evident that $\delta_u\mathrm{Re}^{1/2}$ is constant in Re only for Pr = 0.5 and 0.1. However, $\delta_u\mathrm{Re}^{1/2}$ increases as $\sim \mathrm{Re}^{0.31}$ for large Pr and decreases marginally as $\sim \mathrm{Re}^{-0.07}$ for Pr = 0.02. This shows that for large Pr, δ_u becomes a weak function of Re; this is consistent with the observation of Breuer *et al.*[64] We also plot Grossmann and Lohse's[50] estimate of viscous boundary layer thickness, which is given by $g(\sqrt{\mathrm{Re}_c/\mathrm{Re}})$; here, $g(x) = x(1+x^4)^{-1/4}$ and $\mathrm{Re}_c = 3.401$. It is clear that Grossmann and Lohse's estimate deviates significantly from the actual values.

Therefore, we cannot assume $\delta_u \sim g(\mathrm{Re}^{-1/2})$ for viscous boundary layers in RBC, and it is more prudent to obtain the scaling of $f_2\delta_u^{-1}$ with Ra, where f_2 is the function from Eq. (19). The above deviation from the Prandtl–Blasius profile has also been observed in previous studies.[58,61,62] This is because $\delta_u \sim \mathrm{Re}^{-1/2}$ is valid asymptotically for very large Reynolds numbers.[53]

C. f_i vs Ra for different Pr

In this subsection, we numerically compute f_i using our simulation data and discuss how these quantities vary with Ra for different Pr. We also obtain the limiting cases for the scaling of f_i with Ra.

We numerically compute the total viscous and thermal dissipation rates in the bulk and in the boundary layers for all the simulation runs. Using these values and boundary layer thicknesses, we compute f_1, f_2, f_3, and f_4 and plot them vs Ra in Fig. 3. We observe that f_1 and f_3 are, in general, not constants as in free turbulence. f_1 decreases with Ra except for Pr = 0.1 and 0.02, where it is nearly constant. The above decrease is more prominent for large Pr (≥ 50), where $f_1 \sim \mathrm{Ra}^{-0.35}$. In a similar fashion, f_3 also decreases with Ra for

Published under license by AIP Publishing

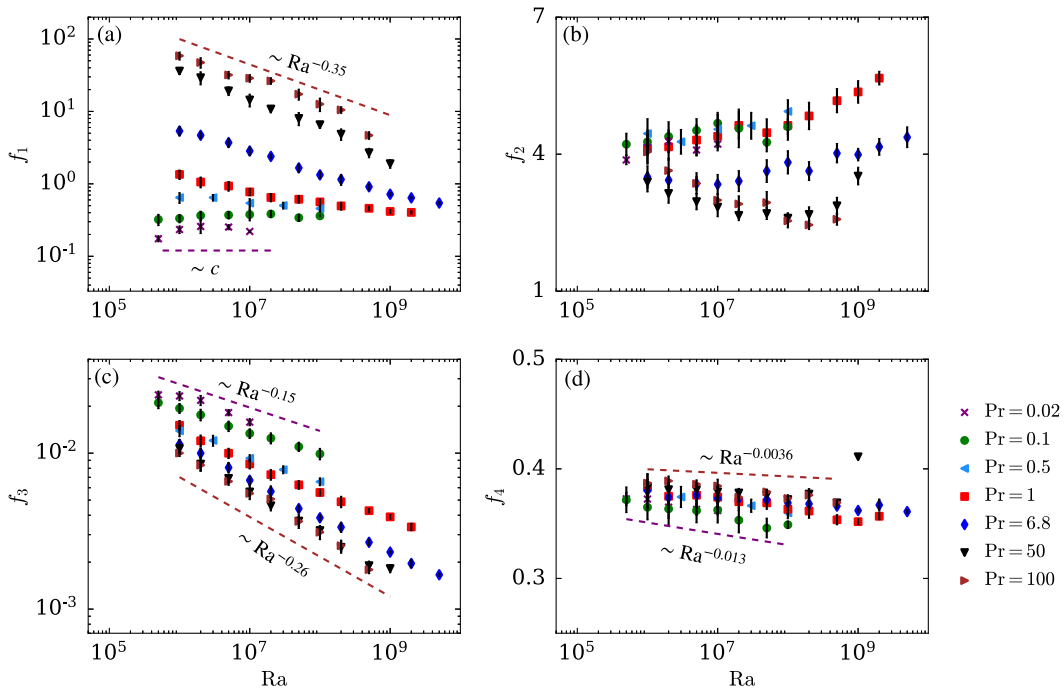

FIG. 3. Plots of (a) f_1, (b) f_2, (c) f_3, and (d) f_4 vs Ra. The error bars represent the standard deviation of the dataset with respect to the temporal average. f_2 remains roughly independent of Ra and Pr, albeit with fluctuations; however, f_1, f_3, and f_4 decrease with Ra.

all Pr values and is more pronounced for large Pr ($f_3 \sim \mathrm{Ra}^{-0.26}$) and less pronounced for small Pr ($f_3 \sim \mathrm{Ra}^{-0.15}$). The above observations imply that the scaling of the dissipation rates in the bulk is similar to that in the entire volume[58,59] (see Sec. IV A). This is because the bulk occupies a large fraction of the total volume, and its contribution to the total dissipation is significant.[58,59]

The Ra and Pr dependences of f_2 cannot be clearly established from Fig. 3(b); we can only infer that f_2 is independent of Ra and Pr, albeit with significant fluctuations. This is consistent with $\epsilon_{u,\mathrm{BL}} \sim \nu U^2/\delta_u^2$ as predicted by Grossmann and Lohse.[49,50] The function f_4 of Fig. 3(d) appears flat, but a careful examination shows that f_4 decreases weakly with Ra, with $f_4 \sim \mathrm{Ra}^{-0.013}$ for small Pr and $f_4 \sim \mathrm{Ra}^{-0.0036}$ for large Pr. The reason for the marginal decrease of f_4 with Ra needs investigation and is not in the scope of this paper.

As discussed earlier, the solution of Eq. (25) for Re and Nu depends on the quantity $f_2\delta_u^{-1}$. Hence, we plot this quantity vs Ra for different Pr in Fig. 4. Since f_2 is nearly constant, $f_2\delta_u^{-1}$ is inversely proportional to the viscous boundary layer thickness. Thus, $f_2\delta_u^{-1}$ increases marginally for large Pr ($\sim \mathrm{Ra}^{0.052}$) and steeply for small Pr ($\sim \mathrm{Ra}^{0.26}$), which is in agreement with the scaling of viscous boundary layer thickness discussed in Sec. IV B.

In Subsection IV D, we describe the machine-learning tools used to determine the functional forms of f_i.

D. Machine-learning algorithm to obtain $f_i(\mathrm{Ra}, \mathrm{Pr})$

So far, we have examined the variation of f_i with only Ra for different Prandtl numbers and obtained the limiting cases. Now, using machine-learning and matching functions, we will combine these scalings to determine f_i as functions of both Ra and Pr. We make use of the machine-learning software WEKA[70] for obtaining the functional forms of f_i. The values of f_i computed for every Ra and Pr using our simulation data serve as training sets for our machine-learning algorithm. For simplicity, we will look for a power-law relation of the form $f_i = A\mathrm{Ra}^{\alpha}\mathrm{Pr}^{\beta}$, take logarithms of this expression, and employ *linear regression* to obtain A, α, and β. The linear regression algorithm works by estimating coefficients for a hyperplane that best fits the training data using the least squares method.

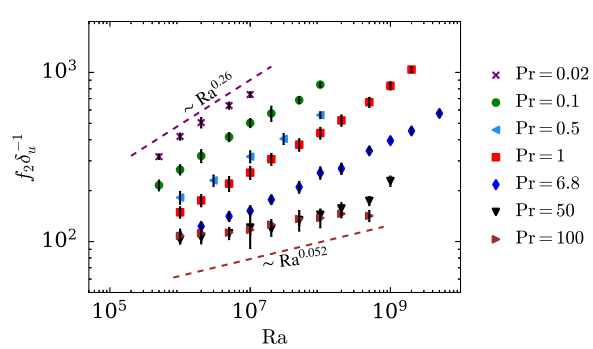

FIG. 4. Plot of $f_2\delta_u^{-1}$ vs Ra. The error bars represent the standard deviation of the dataset with respect to the temporal average. The dependence of $f_2\delta_u^{-1}$ on Ra is stronger for small Pr and becomes weaker as Pr increases.

Published under license by AIP Publishing

Since the dependence of f_i on Ra is not uniform (see Sec. IV C), we split our parameter space into three regimes such that for each regime, the scaling of f_i with Ra is approximately the same. We choose the regimes as follows:

$$\begin{aligned} \text{Small Pr}: &\quad \text{Pr} \le 0.5, \\ \text{Moderate Pr}: &\quad 0.5 \le \text{Pr} \le 6.8, \\ \text{Large Pr}: &\quad \text{Pr} \ge 6.8. \end{aligned}$$

We then determine the prefactor A and the exponents α and β for each regime. To ensure continuity between the regimes, we introduce the following matching functions:

$$H_1(\text{Pr}) = \frac{1}{1 + e^{-k_1(0.5-\text{Pr})}}, \tag{38}$$

$$H_2(\text{Pr}) = \frac{1}{1 + e^{-k_1(\text{Pr}-0.5)}} - \frac{1}{1 + e^{-k_2(\text{Pr}-6.8)}}, \tag{39}$$

$$H_3(\text{Pr}) = \frac{1}{1 + e^{-k_2(\text{Pr}-6.8)}}, \tag{40}$$

where k_1 and k_2 are taken to be 10 and 0.75, respectively. The functions H_1, H_2, and H_3 become unity inside the regimes given by $\text{Pr} < 0.5$, $0.5 < \text{Pr} < 6.8$, and $\text{Pr} > 6.8$, respectively, and become negligible outside their regimes. The value of these functions is 1/2 in the boundaries of their respective regimes. See Fig. 5 for an illustration of the behavior of the matching functions. Using these functions and employing regression for each regime, we obtain the following fits for f_i:

$$f_1 = 0.67H_1\text{Pr}^{0.28} + 27H_2\text{Ra}^{-0.21}\text{Pr}^{0.55} + 170H_3\text{Ra}^{-0.34}\text{Pr}^{0.78}, \tag{41}$$

$$\frac{f_2}{\delta_u} = 4.4H_1\text{Ra}^{0.25}\text{Pr}^{-0.26} + 7.4H_2\text{Ra}^{0.22}\text{Pr}^{-0.29} + 27H_3\text{Ra}^{0.14}\text{Pr}^{-0.18}, \tag{42}$$

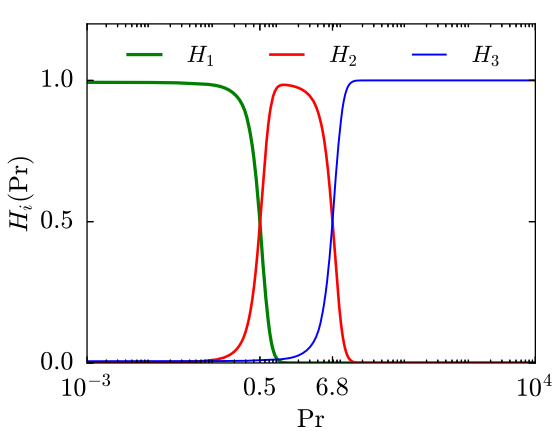

FIG. 5. Plot of the matching functions $H_i(\text{Pr})$ vs Pr. H_1, H_2, and H_3 become unity in the regimes given by $\text{Pr} < 0.5$, $0.5 < \text{Pr} < 6.8$, and $\text{Pr} > 6.8$, respectively. They attain the value of 1/2 at the regime boundaries and become negligible outside their respective regimes.

$$f_3 = 0.095H_1\text{Ra}^{-0.15}\text{Pr}^{-0.17} + 0.25H_2\text{Ra}^{-0.21}\text{Pr}^{-0.17} + 0.45H_3\text{Ra}^{-0.25}\text{Pr}^{-0.093}, \tag{43}$$

$$f_4 = 0.46H_1\text{Ra}^{-0.013}\text{Pr}^{0.010} + 0.43H_2\text{Ra}^{-0.0081}\text{Pr}^{0.0053} + 0.39H_3\text{Ra}^{-0.0036}\text{Pr}^{0.0093}. \tag{44}$$

The average deviation between the f_i's predicted by the fits and the actual values are 24%, 19%, 12%, and 58% for f_1, f_2/δ_u, f_3, and f_4, respectively. As we will see later, incorporation of the aforementioned functional forms results in more accurate predictions than the GL model; thus, the above uncertainty in f_i is acceptable. In the Appendix, we employ the same regression algorithm over a reduced training set consisting of half of our data points and show that the fits so obtained are close to Eqs. (41)–(44). Thus, the estimated parameter values are reasonably robust.

Having obtained the functional forms of f_i, we can plug them in Eqs. (25) and (24) to complete the relation for Re and Nu. We remark that f_i obtained above are valid for RBC cells with a unit aspect ratio. We suspect that they are weak functions of the aspect ratio; this study will be taken up in the future work. Furthermore, efforts are ongoing to make the functional forms of $f_i(\text{Ra}, \text{Pr})$ more compact.

E. Enhancement of the GL model

In this subsection, we will examine the enhancement of the GL model brought about by using the obtained functional forms for the prefactors of the dissipation rates. We will test both, the original GL model and the revised estimates with our numerical results, as well as those of Scheel and Schumacher[11] (Pr = 0.005 and 0.02), Wagner and Shishkina[18] (Pr = 0.7), Emran and Schumacher[17] (Pr = 0.7), Kaczorowski and Xia[19] (Pr = 4.38), and Horn, Shishkina, and Wagner[16] (Pr = 2547.9). We also include the experimental results of Cioni, Ciliberto, and Sommeria[10] (Pr = 0.02), and Niemela *et al.*[32] (Pr = 0.7) for our comparisons. The simulations of Wagner and Shishkina[18] and Kaczorowski and Xia[19] involved a cubical cell such as ours, whereas the rest of the above simulations and experiments involved a cylindrical cell. All the above work involve RBC cells with a unit aspect ratio. We compute the percentage deviations ($\mathcal{D}_{\text{Re}}$ and $\mathcal{D}_{\text{Nu}}$) between the estimated and actual values according to the following formula:

$$\mathcal{D} = \left| \frac{\text{Predicted value} - \text{Actual value}}{\text{Actual value}} \right| \times 100. \tag{45}$$

In Table III, we list the average of the deviations computed for all the points for every Pr.

In Figs. 6(a) and 6(b), we plot the normalized Reynolds number, $\text{Re}\text{Ra}^{-0.5}$, computed using our simulation data and those of Refs. 10, 11, 16–18, and 32, vs Ra. To avoid clutter, we exhibit the results for $\text{Pr} < 1$ in Fig. 6(a) and those for $\text{Pr} \ge 1$ in Fig. 6(b). The dashed and solid curves in Fig. 6 denote Re predicted by the GL model and our revised estimates, respectively. From Fig. 6 and Table III, it is clear that the revised estimates of Re are in better agreement with the observed results compared to the original GL model, especially for extreme Prandtl numbers. Furthermore, the trend of estimated Re is also in better agreement with the numerical and experimental

Published under license by AIP Publishing

TABLE III. Quantitative comparison between the predictions the GL model and the revised estimates of Nu and Re for different sets of simulation and experimental data. $\mathcal{D}_{\mathrm{Re}}$ is the percentage difference between the observed and predicted values of Re, and $\mathcal{D}_{\mathrm{Nu}}$ is the percentage difference between the observed and predicted values of Nu [see Eq. (45)]. Note that no data on Re are available for Pr = 4.38.[19]

Pr	Range of Ra (Re)	$\mathcal{D}_{\mathrm{Re}}$ (Revised estimate) (%)	$\mathcal{D}_{\mathrm{Re}}$ (GL Model) (%)	Range of Ra (Nu)	$\mathcal{D}_{\mathrm{Nu}}$ (Revised estimate) (%)	$\mathcal{D}_{\mathrm{Nu}}$ (GL Model) (%)
0.005	3×10^5–10^7	11	48	3×10^5–10^7	9.6	17
0.02	3×10^5–3×10^9	9.1	62	3×10^5–3×10^9	10	15
0.1	5×10^5–10^8	1.3	30	5×10^5–10^8	3.1	5.0
0.5	10^6–10^8	1.9	14	10^6–10^8	1.4	5.4
0.7	10^5–10^{13}	6.8	25	10^5–10^9	3.8	9.9
1.0	10^6–2×10^9	2.8	20	10^6–2×10^9	3.6	5.8
4.38	...	...	...	10^6–3×10^9	5.7	6.3
6.8	10^6–5×10^9	3.4	27	10^6–5×10^9	5.6	6.5
50	10^6–10^9	6.0	84	10^6–10^9	3.2	7.2
100	10^6–5×10^8	3.4	150	10^6–5×10^8	2.7	3.9
2547.9	10^5–10^9	85	560	10^5–10^9	2.3	17

results (note that the trend of Re computed based on different large-scale velocities does not change even though there may be minor differences in absolute values[1]). This improvement in the estimation of Re is crucial because the predictions of Re are more sensitive to modeling parameters compared to Nu due to a larger range of the scaling exponent.

In Figs. 7(a) and 7(b), we plot the normalized Nusselt number, $\mathrm{NuGr}^{-0.3}$, computed using our simulation data along with those of Refs. 10, 11, and 16–19, vs Ra. We employ the Grashof number Gr = Ra/Pr in the y axis to avoid clutter; this is because Nu ~ $\mathrm{Ra}^{0.3}$ (with a weak dependence on Pr). These figures, along with Table III, indicate that the revised estimates of Nu (solid curves) are more accurate compared to those predicted by the original GL model (dashed curves). It is interesting to note that for extreme

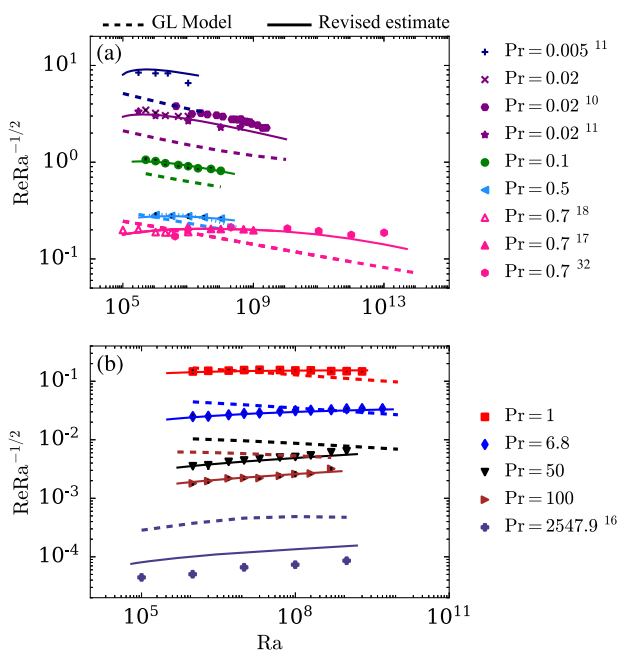

FIG. 6. Comparison between the predictions of Re vs Ra using the original GL model (dashed curves) and our proposed modifications (solid curves) with the results from our work and from the literature[10,11,16–18,32] for (a) Pr < 1 and (b) Pr ≥ 1. The error bars (shown only for our datasets) represent the standard deviation of the dataset with respect to the temporal average.

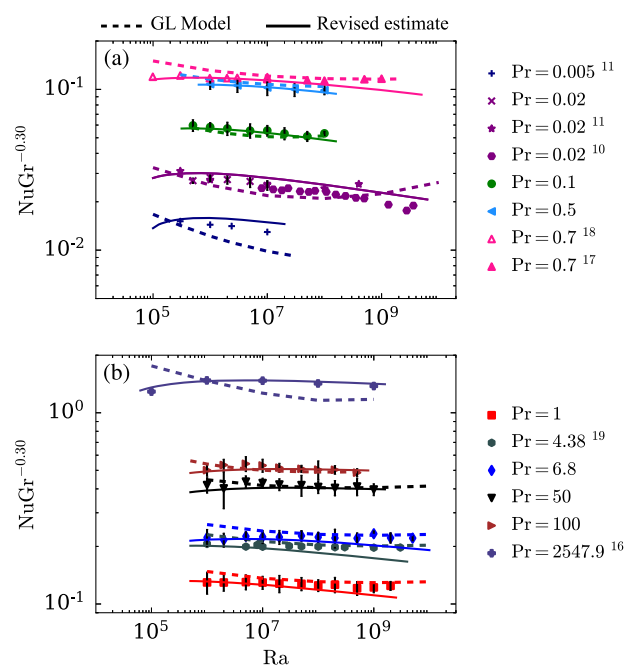

FIG. 7. Comparison between the predictions of Nu vs Ra using the original GL model (dashed curves) and our proposed modifications (solid curves) with the results from our work and from the literature[10,11,16–19] for (a) Pr < 1 and (b) Pr ≥ 1. The error bars (shown only for our datasets) represent the standard deviation of the dataset with respect to the temporal average.

Published under license by AIP Publishing

Prandtl numbers (Pr = 0.005, 2547.9), the accuracy of the revised estimates of Nu is significantly improved with only 2.3% deviation from the actual values for Pr = 2547.9% and 9.6% deviation for Pr = 0.005. Contrast this with the GL model, where we observe 17% deviation for both Pr = 2547.9 and 0.005. For Pr ~ 1, the accuracy of the revised estimates of Nu and those predicted by the GL model are comparable, with the former being more accurate for $\mathrm{Ra} < 10^8$ but marginally less for larger Ra. Thus, we observe an overall improvement in the predictions of Nu, though it is not as significant as it was for Re.

In Figs. 8(a) and 8(b), we contrast the Pr dependence on our estimates of Re and Nu and those of the GL model. Here, we plot the predictions of Re(Pr) and Nu(Pr) along with the actual values computed using our data and those of Refs. 11 and 16–19. We choose four Rayleigh numbers for our comparisons: 10^6, 10^7, 10^8, and 10^9. As expected based on our earlier discussions, the revised estimates of Re(Pr) are more accurate than those of the GL model [see Fig. 8(a)]. We also observe improvements in the predictions of Nu, especially for $\mathrm{Pr} \ll 1$ and $\mathrm{Pr} \gg 1$ [see Fig. 8(b)]. This is again consistent with our earlier discussions.

The improvements, thus, in the predictions of Re and Pr underscore the importance of considering the additional Ra and Pr dependences on the scaling of the dissipation rates and the viscous boundary layers in convection.

F. Limiting cases: Power-law expressions

Recall from Sec. II that Eqs. (22) and (23) reduce to power-law scaling in the limiting cases: $\tilde{D}_{u,\mathrm{bulk}} \gg \tilde{D}_{u,\mathrm{BL}}$ and $\tilde{D}_{u,\mathrm{bulk}} \ll \tilde{D}_{u,\mathrm{BL}}$.

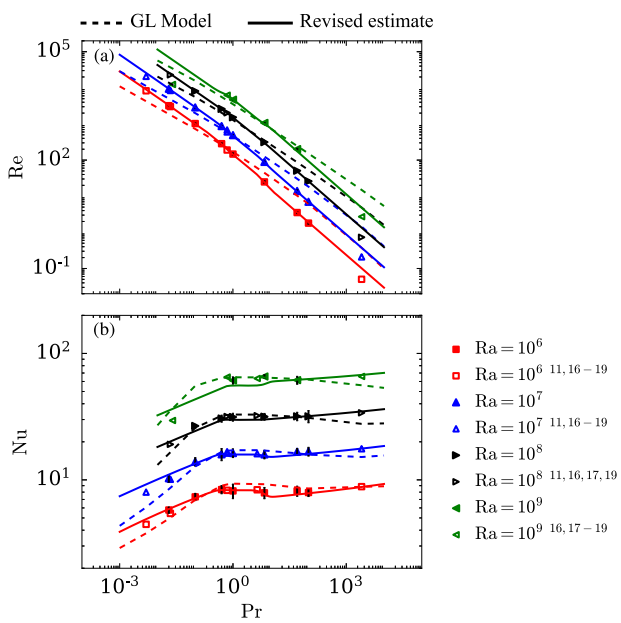

FIG. 8. Comparison between the predictions of (a) Re and (b) Nu vs Pr using the original GL model (dashed curves) and our proposed modifications (solid curves) with the results from our work (filled markers) and from Refs. 11, and 16–19 (unfilled markers). The error bars (shown only for our datasets) represent the standard deviation of the dataset with respect to the temporal average.

First, we will estimate the regimes of Ra and Pr, where the viscous and thermal dissipation rates dominate in the bulk or in the boundary layers. Using f_i's and Eqs. (11)–(14), we deduce that

$$\frac{\tilde{D}_{u,\mathrm{BL}}}{\tilde{D}_{u,\mathrm{bulk}}} = \frac{f_2}{f_1}\frac{d}{\delta_u}\frac{1}{\mathrm{Re}}, \tag{46}$$

$$\frac{\tilde{D}_{T,\mathrm{BL}}}{\tilde{D}_{T,\mathrm{bulk}}} = \frac{2f_4}{f_3}\frac{\mathrm{Nu}}{\mathrm{RePr}}. \tag{47}$$

In Figs. 9(a) and 9(b), we exhibit the plots of the above estimates for Pr = 0.02, 1, and 50. We also exhibit the numerically computed points in Fig. 9; these points are consistent with the estimates given by Eqs. (46) and (47). On the other hand, the ratio of the dissipation rates estimated using the GL model [by employing the bulk and the boundary layer terms of Eqs. (16) and (17)] deviates significantly from the numerically computed points.

The plots show that the thermal dissipation rate in the boundary layers exceeds that in the bulk by a factor of two to four for all Pr values. On the other hand, the viscous dissipation rate in the bulk exceeds that in the boundary layers for $\mathrm{Ra} \gtrsim 10^5$. These observations are in agreement with previous studies.[58,59] The plots imply that $\tilde{D}_{u,\mathrm{BL}}$ dominates $\tilde{D}_{u,\mathrm{bulk}}$ only for $\mathrm{Ra} \ll 10^5$, where $\mathrm{Nu} \approx 1$. However, recall that the power-law relations for this limiting case, given by Eqs. (30) and (31), are invalid for small Nu. Thus, we do not examine this limiting case further.

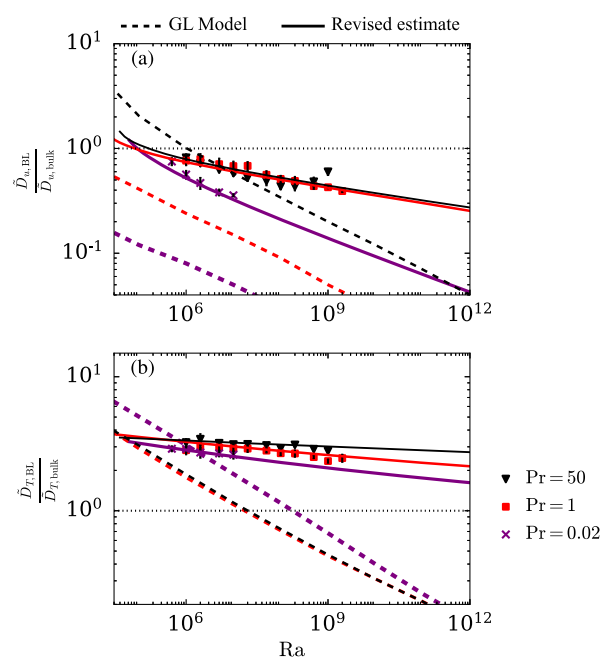

FIG. 9. Estimates of (a) $\tilde{D}_{u,\mathrm{BL}}/\tilde{D}_{u,\mathrm{bulk}}$ and (b) $\tilde{D}_{T,\mathrm{BL}}/\tilde{D}_{T,\mathrm{bulk}}$ using Eqs. (46) and (47) (solid curves) and the GL model (dashed curves) for Pr = 0.02 (purple), Pr = 1 (red), and Pr = 50 (black). Points obtained from our simulation data are also displayed. The dotted horizontal lines in (a) and (b) represent $\tilde{D}_{u,\mathrm{BL}}/\tilde{D}_{u,\mathrm{bulk}} = 1$ and $\tilde{D}_{T,\mathrm{BL}}/\tilde{D}_{T,\mathrm{bulk}} = 1$, respectively. The error bars represent the standard deviation of the dataset with respect to the temporal average.

Published under license by AIP Publishing

For the regimes characterized by $\tilde{D}_{u,\mathrm{bulk}} \gg \tilde{D}_{u,\mathrm{BL}}$, we plug the best-fit relation for f_i in Eqs. (27) and (28) to obtain the following:

$$\mathrm{Re} = \begin{cases} 0.76\mathrm{Ra}^{0.42}\mathrm{Pr}^{-0.72}, & \text{Small Pr}, \\ 0.20\mathrm{Ra}^{0.50}\mathrm{Pr}^{-0.86}, & \text{Moderate Pr}, \\ 0.11\mathrm{Ra}^{0.55}\mathrm{Pr}^{-0.94}, & \text{Large Pr}, \end{cases} \tag{48}$$

$$\mathrm{Nu} = \begin{cases} 0.30\mathrm{Ra}^{0.27}\mathrm{Pr}^{0.11}, & \text{Small Pr}, \\ 0.21\mathrm{Ra}^{0.29}\mathrm{Pr}^{-0.03}, & \text{Moderate Pr}, \\ 0.21\mathrm{Ra}^{0.30}\mathrm{Pr}^{-0.03}, & \text{Large Pr}. \end{cases} \tag{49}$$

Since f_4 is a very weak function of Ra and Pr, we assume it to be a constant (≈ 0.37). The Ra dependence described by Eqs. (48) and (49) is consistent with the scaling observed for large Rayleigh numbers ($10^8 \ll \mathrm{Ra} \ll 10^{12}$) in the literature.[8,11,16–18,22,23,36,57,61,71–73] Furthermore, the above relation for Re and Nu in the small Pr regime is not very far from GL's predictions of $\mathrm{Re} \sim \mathrm{Ra}^{2/5}\mathrm{Pr}^{-3/5}$ and $\mathrm{Nu} \sim \mathrm{Ra}^{1/5}\mathrm{Pr}^{1/5}$. The derived relation for Nu is also in agreement with analytically derived upper bounds of $\mathrm{Nu} \lesssim \mathrm{Ra}^{1/3}\ln(\mathrm{Ra}^{2/3})$[74] and $\mathrm{Nu} \leq 0.644\mathrm{Ra}^{1/3}\ln(\mathrm{Ra}^{1/3})$.[75] Equation (49) also suggests that Nu is a weak function of Pr for moderate and large Pr [see Fig. 8(b)].

For very large Ra ($\gg 10^{12}$), some recent works[48,76] reveal that the Nusselt number scales in the band from $\mathrm{Ra}^{0.33}$ to $\mathrm{Ra}^{0.35}$. Unfortunately, our predictions are not very accurate in this regime; this is because the functional forms of f_i are constructed using data from simulations with $\mathrm{Ra} \lesssim 10^{10}$. Note that for larger Ra, we expect the suppression of viscous and thermal dissipation rates to weaken because of the thin boundary layers. This can, in turn, cause the scaling exponent for Nu to increase. For example, f_1 and f_3 may scale as

$$f_1 \sim \mathrm{Ra}^{-0.14}, \quad f_3 \sim \mathrm{Ra}^{-0.16}, \tag{50}$$

instead of $\mathrm{Ra}^{-0.21}$ as per Eqs. (41) and (43). Plugging the above expressions for f_1 and f_3 in Eq. (28) gives

$$\mathrm{Nu} \sim \mathrm{Ra}^{0.33},$$

which is consistent with the results of Iyer *et al.*[48] However, the scalings for f_1 and f_3, given by Eq. (50), are conjectures that need to be verified using simulations with large Ra's. In a future work, we plan to upgrade our present work by taking inputs from large Ra simulations.

We conclude in Sec. V.

V. CONCLUSIONS

In this paper, we enhance Grossmann and Lohse's model to provide improved predictions of Reynolds and Nusselt numbers in turbulent Rayleigh–Bénard convection. The process of obtaining this relation involves Grossman and Lohse's idea of splitting the total viscous and thermal dissipation rates into bulk and boundary layer contributions and using the exact relations of Shraiman and Siggia. In the present work, we address the additional Ra and Pr dependences on the viscous and thermal dissipation rates in the bulk compared to free turbulence, as well as the deviation of viscous boundary layer thickness from Prandtl–Blasius theory.

The Reynolds and Nusselt numbers are obtained by solving a cubic polynomial equation consisting of four functions $f_i(\mathrm{Ra}, \mathrm{Pr})$ that are prefactors for the dissipation rates in the bulk and boundary layers. Note that these prefactors were constants in the original GL model. The aforementioned functions are determined using machine learning (regression analysis) on 60 datasets obtained from direct numerical simulations of RBC. The cubic polynomial equation reduces to power-law expressions in the limit of the viscous dissipation rate dominating in the bulk.

Using functional forms for the prefactors for the dissipation rates improves the predictions for both Re and Nu compared to the GL model. We observe significant improvements in the predictions of Re, which is important because Re is more sensitive to modeling parameters compared to Nu. The improvement in the predictions of Nu is more pronounced for extreme Pr regimes ($\mathrm{Pr} \leq 0.02$ and ≥ 100). Our results underscore the importance of applying data-driven methods to improve existing models, a practice that has recently been picking up pace in research on turbulence.[77,78] Presently, our work takes inputs from data that are restricted to $\mathrm{Ra} < 10^{10}$ and unit aspect ratio. Our predictions can be further enhanced after determining f_i for $\mathrm{Ra} > 10^{10}$ and for different aspect ratios. Moreover, our work can be extended to convection with magnetic fields following the approach of Zürner *et al.*[79,80]

We believe that our results will be valuable to the scientific and engineering community, especially where flows with extreme Prandtl numbers are involved. For example, they will help understand the fluid dynamics and heat transport in liquid metal batteries that involve small Pr convection.[81] On the other end, our analysis will help strengthen our knowledge on mantle convection, which involves a large Pr flow.[1,2,82] This will, in turn, enable us to make better predictions of seismic disturbances and the earth's magnetic field. Apart from this, our present work should also aid in expanding our knowledge on oceanic and atmospheric flows and, thus, enable us to make improved weather predictions.

ACKNOWLEDGMENTS

The authors thank Arnab Bhattacharya, K. R. Sreenivasan, Jörg Schumacher, and Ambrish Pandey for useful discussions. The authors thank Roshan Samuel, Ali Asad, Soumyadeep Chatterjee, and Syed Fahad Anwer for their contributions to the development of the finite-difference solver SARAS. Our numerical simulations were performed on Shaheen II of KAUST supercomputing laboratory, Saudi Arabia (Project No. k1416) and on HPC2013 of IIT Kanpur, India.

APPENDIX: ROBUSTNESS OF THE ESTIMATED PARAMETER VALUES FOR $f_i(\mathrm{Ra}, \mathrm{Pr})$

In this section, we check the robustness of the parameter values for $f_i(\mathrm{Ra}, \mathrm{Pr})$ estimated in Sec. IV D. Toward this objective, we employ the regression algorithm, used in Sec. IV D, on a reduced training set consisting of 30 data points, which is half of the total number of data points, and test the algorithm on the remaining 30 data points. Starting from the point corresponding to $\mathrm{Pr} = 0.02$ and $\mathrm{Ra} = 5 \times 10^5$, we take alternate data points from Tables I and II for training and the remaining data points for testing. We obtain the

Published under license by AIP Publishing

following fits for f_i for the reduced training set:

$$f_1 = 0.72H_1\mathrm{Pr}^{0.30} + 28H_2\mathrm{Ra}^{-0.21}\mathrm{Pr}^{0.52} + 150H_3\mathrm{Ra}^{-0.33}\mathrm{Pr}^{0.79}, \quad \text{(A1)}$$

$$\frac{f_2}{\delta_u} = 4.1H_1\mathrm{Ra}^{0.26}\mathrm{Pr}^{-0.27} + 6.9H_2\mathrm{Ra}^{0.23}\mathrm{Pr}^{-0.30} + 21H_3\mathrm{Ra}^{0.15}\mathrm{Pr}^{-0.18}, \quad \text{(A2)}$$

$$f_3 = 0.087H_1\mathrm{Ra}^{-0.14}\mathrm{Pr}^{-0.16} + 0.26H_2\mathrm{Ra}^{-0.21}\mathrm{Pr}^{-0.17} + 0.40H_3\mathrm{Ra}^{-0.24}\mathrm{Pr}^{-0.095}, \quad \text{(A3)}$$

$$f_4 = 0.45H_1\mathrm{Ra}^{-0.012}\mathrm{Pr}^{0.0075} + 0.42H_2\mathrm{Ra}^{-0.0078}\mathrm{Pr}^{0.0050} + 0.36H_3\mathrm{Pr}^{0.0161}. \quad \text{(A4)}$$

We observe that the fits given by Eqs. (A1)–(A4) are similar to those of Eqs. (41)–(44), which correspond to the fits obtained when all the data points were used as training sets. The average deviation between the f_i's predicted by the fits and the actual values of the test set are 25%, 20%, 13%, and 71% for f_1, f_2/δ_u, f_3, and f_4, respectively. These deviations are almost the same as those observed when all the datasets were used for training and testing. Furthermore, if we train our algorithm using only 15 datasets (every fourth set from Tables I and II), we obtain

$$f_1 = 0.68H_1\mathrm{Pr}^{0.31} + 25H_2\mathrm{Ra}^{-0.20}\mathrm{Pr}^{0.47} + 238H_3\mathrm{Ra}^{-0.37}\mathrm{Pr}^{0.81}, \quad \text{(A5)}$$

$$\frac{f_2}{\delta_u} = 3.7H_1\mathrm{Ra}^{0.26}\mathrm{Pr}^{-0.27} + 5.8H_2\mathrm{Ra}^{0.24}\mathrm{Pr}^{-0.33} + 23H_3\mathrm{Ra}^{0.15}\mathrm{Pr}^{-0.19}, \quad \text{(A6)}$$

$$f_3 = 0.060H_1\mathrm{Ra}^{-0.12}\mathrm{Pr}^{-0.17} + 0.23H_2\mathrm{Ra}^{-0.20}\mathrm{Pr}^{-0.19} + 0.40H_3\mathrm{Ra}^{-0.24}\mathrm{Pr}^{-0.090}, \quad \text{(A7)}$$

$$f_4 = 0.42H_1\mathrm{Ra}^{-0.0099} + 0.41H_2\mathrm{Ra}^{-0.0069}\mathrm{Pr}^{0.0059} + 0.38H_3, \quad \text{(A8)}$$

with the average deviation between the f_i's predicted by the fits and the actual values of the test set being 26%, 21%, 16%, and 71% for f_1, f_2/δ_u, f_3, and f_4, respectively. We observe that there are visible changes in the parameter values estimated using 15 datasets. Thus, we infer that the parameter values estimated using more than 30 datasets are reasonably robust.

DATA AVAILABILITY

The data that support the findings of this study are available from the corresponding author upon reasonable request.

REFERENCES

[1] G. Ahlers, S. Grossmann, and D. Lohse, "Heat transfer and large scale dynamics in turbulent Rayleigh-Bénard convection," Rev. Mod. Phys. **81**, 503–537 (2009).
[2] F. Chillà and J. Schumacher, "New perspectives in turbulent Rayleigh-Bénard convection," Eur. Phys. J. E **35**, 58 (2012).
[3] E. D. Siggia, "High Rayleigh number convection," Annu. Rev. Fluid Mech. **26**, 137–168 (1994).
[4] K.-Q. Xia, "Current trends and future directions in turbulent thermal convection," Theor. Appl. Mech. Lett. **3**, 052001 (2013).
[5] M. K. Verma, *Physics of Buoyant Flows: From Instabilities to Turbulence* (World Scientific, Singapore, 2018).
[6] W. V. R. Malkus, "The heat transport and spectrum of thermal turbulence," Proc. R. Soc. London, Ser. A **225**, 196–212 (1954).
[7] R. H. Kraichnan, "Turbulent thermal convection at arbitrary Prandtl number," Phys. Fluids **5**, 1374–1389 (1962).
[8] B. Castaing, G. Gunaratne, F. Heslot, L. Kadanoff, A. Libchaber, S. Thomae, X.-Z. Wu, S. Zaleski, and G. Zanetti, "Scaling of hard thermal turbulence in Rayleigh-Bénard convection," J. Fluid Mech. **204**, 1–30 (1989).
[9] B. I. Shraiman and E. D. Siggia, "Heat transport in high-Rayleigh-number convection," Phys. Rev. A **42**, 3650–3653 (1990).
[10] S. Cioni, S. Ciliberto, and J. Sommeria, "Strongly turbulent Rayleigh-Bénard convection in mercury: Comparison with results at moderate Prandtl number," J. Fluid Mech. **335**, 111–140 (1997).
[11] J. D. Scheel and J. Schumacher, "Predicting transition ranges to fully turbulent viscous boundary layers in low Prandtl number convection flows," Phys. Rev. Fluids **2**, 123501 (2017).
[12] H. T. Rossby, "A study of Bénard convection with and without rotation," J. Fluid Mech. **36**, 309–335 (1969).
[13] T. Takeshita, T. Segawa, J. A. Glazier, and M. Sano, "Thermal turbulence in mercury," Phys. Rev. Lett. **76**, 1465–1468 (1996).
[14] S. Ashkenazi and V. Steinberg, "High Rayleigh number turbulent convection in a gas near the gas-liquid critical point," Phys. Rev. Lett. **83**, 3641–3645 (1999).
[15] X. Chavanne, F. Chillà, B. Castaing, B. Hébral, B. Chabaud, and J. Chaussy, "Observation of the ultimate regime in Rayleigh-Bénard convection," Phys. Rev. Lett. **79**, 3648–3651 (1997).
[16] S. Horn, O. Shishkina, and C. Wagner, "On non-Oberbeck-Boussinesq effects in three-dimensional Rayleigh-Bénard convection in glycerol," J. Fluid Mech. **724**, 175–202 (2013).
[17] M. S. Emran and J. Schumacher, "Fine-scale statistics of temperature and its derivatives in convective turbulence," J. Fluid Mech. **611**, 13–34 (2008).
[18] S. Wagner and O. Shishkina, "Aspect-ratio dependency of Rayleigh-Bénard convection in box-shaped containers," Phys. Fluids **25**, 085110 (2013).
[19] M. Kaczorowski and K.-Q. Xia, "Turbulent flow in the bulk of Rayleigh-Bénard convection: Small-scale properties in a cubic cell," J. Fluid Mech. **722**, 596–617 (2013).
[20] J. J. Niemela and K. R. Sreenivasan, "Confined turbulent convection," J. Fluid Mech. **481**, 355–384 (2003).
[21] D. Funfschilling, E. Brown, A. Nikolaenko, and G. Ahlers, "Heat transport by turbulent Rayleigh-Bénard convection in cylindrical samples with aspect ratio one and larger," J. Fluid Mech. **536**, 145–154 (2005).
[22] A. Pandey and M. K. Verma, "Scaling of large-scale quantities in Rayleigh-Bénard convection," Phys. Fluids **28**, 095105 (2016).
[23] A. Pandey, A. Kumar, A. G. Chatterjee, and M. K. Verma, "Dynamics of large-scale quantities in Rayleigh-Bénard convection," Phys. Rev. E **94**, 053106 (2016).
[24] A. Pandey, M. K. Verma, and P. K. Mishra, "Scaling of heat flux and energy spectrum for very large Prandtl number convection," Phys. Rev. E **89**, 023006 (2014).
[25] R. J. A. M. Stevens, R. Verzicco, and D. Lohse, "Radial boundary layer structure and Nusselt number in Rayleigh–Bénard convection," J. Fluid Mech. **643**, 495–507 (2010).
[26] A. Xu, L. She, and H.-D. Xi, "Statistics of temperature and thermal energy dissipation rate in low-Prandtl number turbulent thermal convection," Phys. Fluids **31**, 125101 (2019).
[27] D.-L. Dong, B.-F. Wang, Y.-H. Dong, Y.-X. Huang, N. Jiang, Y.-L. Liu, Z.-M. Lu, X. Qiu, Z.-Q. Tang, and Q. Zhou, "Influence of spatial arrangements of roughness elements on turbulent Rayleigh-Bénard convection," Phys. Fluids **32**, 045114 (2020).
[28] U. Madanan and R. J. Goldstein, "High-Rayleigh-number thermal convection of compressed gases in inclined rectangular enclosures," Phys. Fluids **32**, 017103 (2020).

Published under license by AIP Publishing

[29]M. Vial and R. H. Hernández, "Feedback control and heat transfer measurements in a Rayleigh-Bénard convection cell," Phys. Fluids **29**, 074103 (2017).
[30]K.-Q. Xia, S. Lam, and S.-Q. Zhou, "Heat-flux measurement in high-Prandtl-number turbulent Rayleigh-Bénard convection," Phys. Rev. Lett. **88**, 064501 (2002).
[31]R. Verzicco and R. Camussi, "Prandtl number effects in convective turbulence," J. Fluid Mech. **383**, 55–73 (1999).
[32]J. J. Niemela, L. Skrbek, K. R. Sreenivasan, and R. J. Donnelly, "The wind in confined thermal convection," J. Fluid Mech. **449**, 169–178 (2001).
[33]S. Lam, X.-D. Shang, S.-Q. Zhou, and K.-Q. Xia, "Prandtl number dependence of the viscous boundary layer and the Reynolds numbers in Rayleigh-Bénard convection," Phys. Rev. E **65**, 066306 (2002).
[34]M. K. Verma, P. K. Mishra, A. Pandey, and S. Paul, "Scalings of field correlations and heat transport in turbulent convection," Phys. Rev. E **85**, 016310 (2012).
[35]G. Silano, K. R. Sreenivasan, and R. Verzicco, "Numerical simulations of Rayleigh-Bénard convection for Prandtl numbers between 10^{-1} and 10^{4} and Rayleigh numbers between 10^{5} and 10^{9}," J. Fluid Mech. **662**, 409–446 (2010).
[36]E. Brown, D. Funfschilling, and G. Ahlers, "Anomalous Reynolds-number scaling in turbulent Rayleigh-Bénard convection," J. Stat. Mech.: Theory Exp. **2007**, P10005.
[37]D. Lohse and F. Toschi, "Ultimate state of thermal convection," Phys. Rev. Lett. **90**, 034502 (2003).
[38]X. He, D. Funfschilling, E. Bodenschatz, and G. Ahlers, "Heat transport by turbulent Rayleigh–Bénard convection for Pr ≈ 0.8 and $4 \times 10^{11} \leq \mathrm{Ra} \leq 2 \times 10^{14}$: Ultimate-state transition for aspect ratio $T = 1.00$," New J. Phys. **14**, 063030 (2012).
[39]S. S. Pawar and J. H. Arakeri, "Kinetic energy and scalar spectra in high Rayleigh number axially homogeneous buoyancy driven turbulence," Phys. Fluids **28**, 065103 (2016).
[40]S. S. Pawar and J. H. Arakeri, "Two regimes of flux scaling in axially homogeneous turbulent convection in vertical tube," Phys. Rev. Fluids **1**, 042401(R) (2016).
[41]L. E. Schmidt, E. Calzavarini, D. Lohse, and F. Toschi, "Axially homogeneous Rayleigh-Bénard convection in a cylindrical cell," J. Fluid Mech. **691**, 52–68 (2012).
[42]E. Calzavarini, D. Lohse, F. Toschi, and R. Tripiccione, "Rayleigh and Prandtl number scaling in the bulk of Rayleigh–Bénard turbulence," Phys. Fluids **17**, 055107 (2005).
[43]E. Calzavarini, C. R. Doering, J. D. Gibbon, D. Lohse, A. Tanabe, and F. Toschi, "Exponentially growing solutions in homogeneous Rayleigh-Bénard convection," Phys. Rev. E **73**, 035301 (2006).
[44]C. R. Doering, "Thermal forcing and 'classical' and 'ultimate' regimes of Rayleigh–Bénard convection," J. Fluid Mech. **868**, 1–4 (2019).
[45]P.-E. Roche, B. Castaing, B. Chabaud, and B. Hebral, "Observation of the 1/2 power law in Rayleigh–Bénard convection," Phys. Rev. E **63**, 045303(R) (2001).
[46]G. Ahlers, D. Funfschilling, and E. Bodenschatz, "Transitions in heat transport by turbulent convection at Rayleigh numbers up to 10^{15}," New J. Phys. **11**, 123001 (2009).
[47]J. J. Niemela, L. Skrbek, K. R. Sreenivasan, and R. J. Donnelly, "Turbulent convection at very high Rayleigh numbers," Nature **404**, 837–840 (2000).
[48]K. P. Iyer, J. D. Scheel, J. Schumacher, and K. R. Sreenivasan, "Classical 1/3 scaling of convection holds up to $\mathrm{Ra} = 10^{15}$," Proc. Natl. Acad. Sci. U. S. A. **117**, 7594–7598 (2020).
[49]S. Grossmann and D. Lohse, "Scaling in thermal convection: A unifying theory," J. Fluid Mech. **407**, 27–56 (2000).
[50]S. Grossmann and D. Lohse, "Thermal convection for large Prandtl numbers," Phys. Rev. Lett. **86**, 3316–3319 (2001).
[51]S. Grossmann and D. Lohse, "Prandtl and Rayleigh number dependence of the Reynolds number in turbulent thermal convection," Phys. Rev. E **66**, 016305 (2002).
[52]S. Grossmann and D. Lohse, "On geometry effects in Rayleigh-Bénard convection," J. Fluid Mech. **486**, 105–114 (2003).
[53]L. D. Landau and E. M. Lifshitz, *Fluid Mechanics*, 2nd ed., Course of Theoretical Physics (Elsevier, Oxford, 1987).
[54]R. J. A. M. Stevens, E. P. van der Poel, S. Grossmann, and D. Lohse, "The unifying theory of scaling in thermal convection: The updated prefactors," J. Fluid Mech. **730**, 295–308 (2013).
[55]M. Lesieur, *Turbulence in Fluids* (Springer-Verlag, Dordrecht, 2008).
[56]M. K. Verma, *Energy Trasnfers in Fluid Flows: Multiscale and Spectral Perspectives* (Cambridge University Press, Cambridge, 2019).
[57]R. Verzicco and R. Camussi, "Numerical experiments on strongly turbulent thermal convection in a slender cylindrical cell," J. Fluid Mech. **477**, 19–49 (2003).
[58]S. Bhattacharya, A. Pandey, A. Kumar, and M. K. Verma, "Complexity of viscous dissipation in turbulent thermal convection," Phys. Fluids **30**, 031702 (2018).
[59]S. Bhattacharya, R. Samtaney, and M. K. Verma, "Scaling and spatial intermittency of thermal dissipation in turbulent convection," Phys. Fluids **31**, 075104 (2019).
[60]S. Bhattacharya, S. Sadhukhan, A. Guha, and M. K. Verma, "Similarities between the structure functions of thermal convection and hydrodynamic turbulence," Phys. Fluids **31**, 115107 (2019).
[61]J. D. Scheel, E. Kim, and K. R. White, "Thermal and viscous boundary layers in turbulent Rayleigh–Bénard convection," J. Fluid Mech. **711**, 281–305 (2012).
[62]N. Shi, M. S. Emran, and J. Schumacher, "Boundary layer structure in turbulent Rayleigh–Bénard convection," J. Fluid Mech. **706**, 5–33 (2012).
[63]S. Chandrasekhar, *Hydrodynamic and Hydromagnetic Stability* (Dover Publications, Oxford, 1981).
[64]M. Breuer, S. Wessling, J. Schmalzl, and U. Hansen, "Effect of inertia in Rayleigh-Bénard convection," Phys. Rev. E **69**, 026302 (2004).
[65]G. K. Batchelor, "Small-scale variation of convected quantities like temperature in turbulent fluid. Part 1. General discussion and the case of small conductivity," J. Fluid Mech. **5**, 113–133 (1959).
[66]M. K. Verma, R. J. Samuel, S. Chatterjee, S. Bhattacharya, and A. Asad, "Challenges in fluid flow simulations using exascale computing," SN Comput. Sci. **1**, 178 (2020).
[67]R. J. Samuel, S. Bhattacharya, A. Asad, S. Chatterjee, M. K. Verma, R. Samtaney, and S. F. Anwer, "SARAS: A general-purpose PDE solver for fluid dynamics," J. Open Source Software (unpublished) (2020).
[68]G. Grötzbach, "Spatial resolution requirements for direct numerical simulation of the Rayleigh-Bénard convection," J. Comput. Phys. **49**, 241–264 (1983).
[69]M. K. Verma, S. Alam, and S. Chatterjee, "Turbulent drag reduction in magnetohydrodynamic and quasi-static magnetohydrodynamic turbulence," Phys. Plasmas **27**, 052301 (2020).
[70]E. Frank, M. Hall, G. Holmes, R. Kirkby, B. Pfahringer, I. H. Witten, and L. Trigg, "Weka—A machine learning workbench for data mining," in *Data Mining and Knowledge Discovery Handbook* (Springer, 2009), pp. 1269–1277.
[71]X.-L. Qiu and P. Tong, "Temperature oscillations in turbulent Rayleigh-Bénard convection," Phys. Rev. E **66**, 026308 (2002).
[72]A. Nikolaenko, E. Brown, D. Funfschilling, and G. Ahlers, "Heat transport by turbulent Rayleigh-Bénard convection in cylindrical cells with aspect ratio one and less," J. Fluid Mech. **523**, 251–260 (2005).
[73]J. D. Scheel and J. Schumacher, "Local boundary layer scales in turbulent Rayleigh-Bénard convection," J. Fluid Mech. **758**, 344–373 (2014).
[74]P. Constantin and C. R. Doering, "Infinite Prandtl number convection," J. Stat. Phys. **94**, 159–172 (1999).
[75]C. R. Doering, F. Otto, and M. G. Reznikoff, "Bounds on vertical heat transport for infinite-Prandtl-number Rayleigh-Bénard convection," J. Fluid Mech. **560**, 229–241 (2006).
[76]X. Zhu, V. Mathai, R. J. A. M. Stevens, R. Verzicco, and D. Lohse, "Transition to the ultimate regime in two-dimensional Rayleigh-Bénard convection," Phys. Rev. Lett. **120**, 144502 (2018).
[77]S. Pandey, J. Schumacher, and K. R. Sreenivasan, "A perspective on machine learning in turbulent flows," J. Turbul. **21**, 567–584 (2020).
[78]E. J. Parish and K. Duraisamy, "A paradigm for data-driven predictive modeling using field inversion and machine learning," J. Comput. Phys. **305**, 758–774 (2016).

Published under license by AIP Publishing

[79] T. Zürner, W. Liu, D. Krasnov, and J. Schumacher, "Heat and momentum transfer for magnetoconvection in a vertical external magnetic field," Phys. Rev. E **94**, 043108 (2016).
[80] T. Zürner, "Refined mean field model of heat and momentum transfer in magnetoconvection," Phys. Fluids **32**, 107101 (2020).
[81] D. H. Kelley and T. Weier, "Fluid mechanics of liquid metal batteries," Appl. Mech. Rev. **70**, 020801 (2018).
[82] V. N. Prakash, K. R. Sreenivas , and J. H. Arakeri, "The role of viscosity contrast on plume structure in laboratory modeling of mantle convection," Chem. Eng. Sci. **158**, 245–256 (2017).

Published under license by AIP Publishing